PHOTONICS Research

Carrier dynamic process in all-inorganic halide perovskites explored by photoluminescence spectra

Jing Chen,[1] Chao Zhang,[1] Xiaolin Liu,[1] Lin Peng,[1] Jia Lin,[1,*] and Xianfeng Chen[2,3]

[1]Department of Physics, Shanghai Key Laboratory of Materials Protection and Advanced Materials in Electric Power, Shanghai University of Electric Power, Shanghai 200090, China
[2]State Key Laboratory of Advanced Optical Communication Systems and Networks, School of Physics and Astronomy, Shanghai Jiao Tong University, Shanghai 200240, China
[3]Collaborative Innovation Center of Light Manipulation and Applications, Shandong Normal University, Jinan 250358, China
*Corresponding author: jlin@shiep.edu.cn

Received 25 September 2020; revised 10 November 2020; accepted 25 November 2020; posted 30 November 2020 (Doc. ID 410290); published 25 January 2021

Recently, all-inorganic halide perovskites have received enormous attention because of their excellent optoelectronic properties. Among them, the power conversion efficiency (PCE) of all-inorganic halide perovskite solar cells has made rapid progress in the last few years. However, understanding the intrinsic physical nature of halide perovskites, especially the dynamic process of photo-generated carriers, is a key for improving the PCE. In this review, we introduced and summarized the photoluminescence (PL) technique used to explore the carrier dynamic process in all-inorganic halide perovskites. Several physical models were proposed to investigate the dynamic parameters, i.e., recombination lifetime and diffusion length, by analyzing the steady-state PL as well as the time-resolved PL spectra. We also discussed the distinction of PL spectral behavior between bulk halide perovskite samples and those grown with transport layers due to the participation of different dominant dynamic paths. Finally, we briefly described some other optical techniques reported to study the relevant physical properties of all-inorganic halide perovskites.

https://doi.org/10.1364/PRJ.410290

1. INTRODUCTION

Halide perovskite materials have developed rapidly due to their exceptional optoelectronic properties and low-cost fabrication processes. The initial studies were focused on organic–inorganic hybrid perovskites; however, up to now, they still go through some compositional and structural degradation mechanisms, leading to thermal and chemical instabilities [1–7]. To realize future commercialization, we need to pursue low cost, high efficiency, and high stability, which is inseparable from the excellent performance of the material. Fortunately, all-inorganic halide perovskites display both high stability and remarkable optoelectronic properties, with long carrier recombination lifetime [8–11], long diffusion length [12,13], and strong optical absorption [14], which render them as an intriguing and promising semiconductor for a broad range of applications including perovskite solar cells (PSCs), photodetectors, light-emitting diodes (LEDs), and lasing [15–25]. These properties have led to rapid increases in the efficiency of PSCs and LEDs over a short period of time [26].

The study of carrier dynamics in all-inorganic halide perovskites, i.e., recombination and transport, is necessary to better understand their photoelectronic applications. Therefore, the relevant physical parameters are usually measured and discussed in the newly grown halide perovskite samples by different techniques, among which photoluminescence (PL) is widely employed. As we know, the dynamic process of carriers in semiconductor materials is rather complex, especially in the non-equilibrium state. The photo-generated carriers will go through several paths such as recombination and diffusion. By using steady-state PL (SSPL) and time-resolved PL (TRPL) techniques, researchers have established theoretical models, which can be utilized to deeply analyze the dynamic process inside the materials. Although the PL technique has been widely used to explore the dynamic physics of all-inorganic halide perovskites recently, there is no systematic report on it up to now. Moreover, we should be aware that the PL characteristics as well as the corresponding conclusions may be completely opposite for the samples with or without carrier transport layers (TLs). This is what often confused people.

In this work, we reviewed the investigation of the carrier dynamic process of all-inorganic halide perovskite materials using the PL technique. This article is divided into four parts: in

the first section, we introduced the overall existed carrier dynamics in halide perovskite materials, including recombination and transport; in the second section, we presented the application of SSPL and TRPL to the study of the carrier relaxation process in all-inorganic halide perovskites; in the third part, carrier dynamics in all-inorganic halide perovskites with TLs through a PL experiment were discussed in detail, where we focused on the efficiency of photo-induced carrier transfer into the electron (or hole) TL, and the way to obtain diffusion coefficient and length was also demonstrated; finally, we briefly discussed the limitation of PL spectra and introduced other techniques employed to study carrier lifetime. Throughout the whole article, in addition to reviewing the application of PL spectra in the analysis of carrier dynamics, the corresponding data and conclusions of all-inorganic halide perovskite materials reported in recent years were also summarized and discussed.

2. CARRIER DYNAMIC PROCESS IN SEMICONDUCTORS

Typically, in most semiconductor materials, carrier dynamics mainly refer to two processes: recombination and transport. As for recombination, there are three different routes after carrier excitation by absorption: radiative recombination, non-radiative Shockley–Read–Hall (SRH) recombination, and Auger recombination. They are also related to the monomolecular, bi-molecular, and tri-molecular processes of optical relaxation, respectively. In the radiative recombination event, an electron–hole pair is annihilated to emit the photon and thus generate the PL signal. The SRH recombination is related to the presence of defects. The excited carriers are captured by the defect sites, and then they gradually relax towards the ground state (GS) by the emission of phonons. The process of Auger recombination involves non-radiative transfer of the excess energy due to electron–hole recombination to a third charge carrier (electron or hole), which is ejected from its original state.

The above depicted carrier dynamic processes are also included in all-inorganic halide perovskite materials, and these processes may be more complicated and have not been investigated thoroughly up to now. As shown in Fig. 1, when the energy of the absorbed photon is larger than the band gap energy, the electron will transit to the higher excitonic state (ES, green dashed line), and then it cools down to the ES rapidly within 10 ps [27,28]. After that, the electron may go through different decay paths. It can combine directly with the free hole in the GS with simultaneous PL emission, i.e., radiative recombination, and the decay time is about hundreds of picoseconds (ps) to dozens of nanoseconds (ns) [27,29], as shown by the red solid line with an arrow in Fig. 1. In addition, there are always defect states [30,31], surface states [32,33], or dark states [34,35] existing in the all-inorganic halide perovskites, which are named and referred to as trap states (TS) henceforth [36–38]. The photo-excited electrons on the ES could also be trapped by these TS within 50 ps (red dashed line with arrow). These trapped electrons may be combined directly with the holes in GS (blue solid line with arrow) or with the holes also captured by TS (green solid line with arrow). It is also observed that the trapped electrons could be detrapped back to the ES under thermal activation to become free electrons (purple dashed line with arrow), then followed by the radiative recombination again with holes in the GS [34,39]. In addition, photo-generated carriers will also participate in the transport process, that is, diffusion caused by concentration gradient or drift under the electric field. Here, we use the yellow curve with an arrow to represent the transport in Fig. 1.

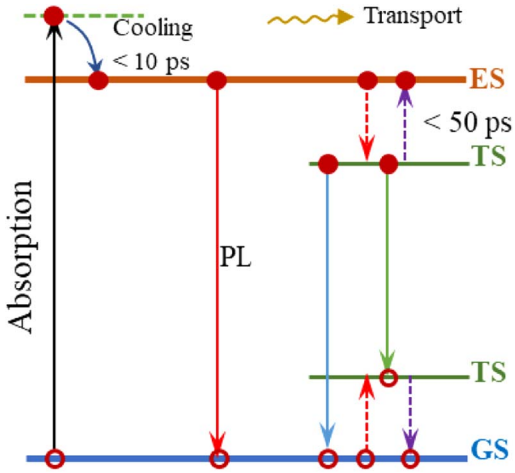

Fig. 1. Carrier dynamic model.

3. CARRIER RECOMBINATION DECAY IN ALL-INORGANIC HALIDE PEROVSKITES BY PL SPECTRA

A. SSPL

PL spectroscopy is a keystone characterization technique to explore properties of the carrier relaxation process [40]. Most of the grown all-inorganic halide perovskites employed this special method to characterize the properties of the materials. For the SSPL spectrum, the position of the peak refers to the band gap energy, which corresponds to the absorption edge. Furthermore, the full width at half-maximum (FWHM) of the peak as well as the band tail can qualitatively reflect the homogeneity of the material. Besides that, the information of the carrier recombination process can also be extracted by the SSPL spectrum, and this is the focus of our discussion below.

The mechanism of recombination can be estimated by the power dependence of the steady-state integrated PL intensity I_{PL} and the excitation density I_{ex} as $I_{PL} \propto I_{ex}^{k}$ [41]. It reveals a linear relationship in a log–log plot, and the fitted slope of this line is k, by which the recombination mechanism can be determined qualitatively. There is a long-standing controversy whether free carriers or excitons are generated in perovskites upon photoexcitation. Thus, the k value is helpful to study the competition between exciton and free carrier: $k = 2$ for free carrier recombination, $1 < k < 2$ for recombination of excitons, and $k < 1$ for free-to-bound recombination [42]. Another viewpoint is proposed by Saba *et al.* according to a trap-assisted recombination model, that k should equal 1.5 when the majority of TS were unoccupied, and it gradually decreased to 1 when the trap density decreased [43]. Later,

Chirvony *et al.* pointed out that if the PL intensity dependence with $k = 1$ was observed, then it implied that the PL quantum yield (PLQY) remained constant [34]. Recently, a more intuitive argument was declared [40]. As it indicated, the two basic patterns are expected: mono-molecular, i.e., linear, and bi-molecular, that in some conditions translates into quadratic dependence. As it argued, in some cases, the intermediate case (k between 1 and 2), i.e., mixture of these two, is expected.

Shi *et al.* investigated the SSPL with various excitation powers at room temperature in $CsPbBr_3$ nanocrystals (NCs) [27]. The average excitation power was controlled from 4 μW to 18 mW. As shown in Fig. 2(a), I_{PL} showed a linear relationship with the excitation laser power I_{ex}, and the slope was about 1.34. With increasing excitation power, no saturation effect or rapid increase was observed, which means that the PL was mainly due to the spontaneous radiation rather than amplified spontaneous emission or other optical nonlinear phenomena [44,45]. Figure 2(b) plots the PL intensity dependence on the excitation power of the pristine $CsPbBr_3$ film and trioctylphosphine oxide (TOPO)-treated $CsPbBr_3$ film [46], with a power-law exponent of 1.41 and 1.30, respectively. As we have mentioned above, the pristine film had a relatively high k value of 1.41, meaning that there were more TS on the pristine film surface or grain boundaries. From this point of view, the decrease of k in the TOPO-treated film offered evidence that there were fewer non-radiative pathways, and the introduced TOPO played an important role in passivating non-radiative defects in $CsPbBr_3$ films.

Power-dependent PL intensity was also effective for studying lasing properties, which is a very important application of all-inorganic perovskites. Among them, the $CsPbBr_3$ nanowires/nanoribbons are one of the most competitive materials [25,47,48]. For example, Fig. 2(c) exhibits the power-dependent emission spectra of an individual $CsPbBr_3$ nanowire, and Fig. 2(d) shows the plot of the intensity and the FWHM of emission peaks versus the excitation power [47]. A typical "S" curve revealed in Fig. 2(d) indicates the transition processes from spontaneous emission to the full lasing status. Meanwhile, at the lasing threshold of 16.71 $\mu J/cm^2$, a sharp decrease in the FWHM is observed. By fitting the lasing rate equation, the spontaneous emission factor can be obtained, which has a certain reference guideline for lasing investigation.

B. TRPL Techniques

To deeply investigate the carrier recombination mechanism as well as the lifetime, TRPL is then widely employed. As we know, the intensity of PL is the direct reflection of carrier radiative recombination. In a nonequilibrium situation, recombination is proportional to the concentration of minority carriers, i.e., for n-type material, $R = -\frac{p}{\tau_p}$, where R is the recombination rate, and τ_p is the lifetime of holes. Since the carrier density changes with time, the PL intensity is also a function of time. If the carriers only suffer radiative recombination, the dependency of PL intensity on the time satisfies the relationship $I_{PL}(t) = Ae^{-\frac{t}{\tau}} + y_0$, where τ is the lifetime of radiative recombination. For a more intuitive understanding of how lifetime τ affects TRPL curves, we calculated the TRPL

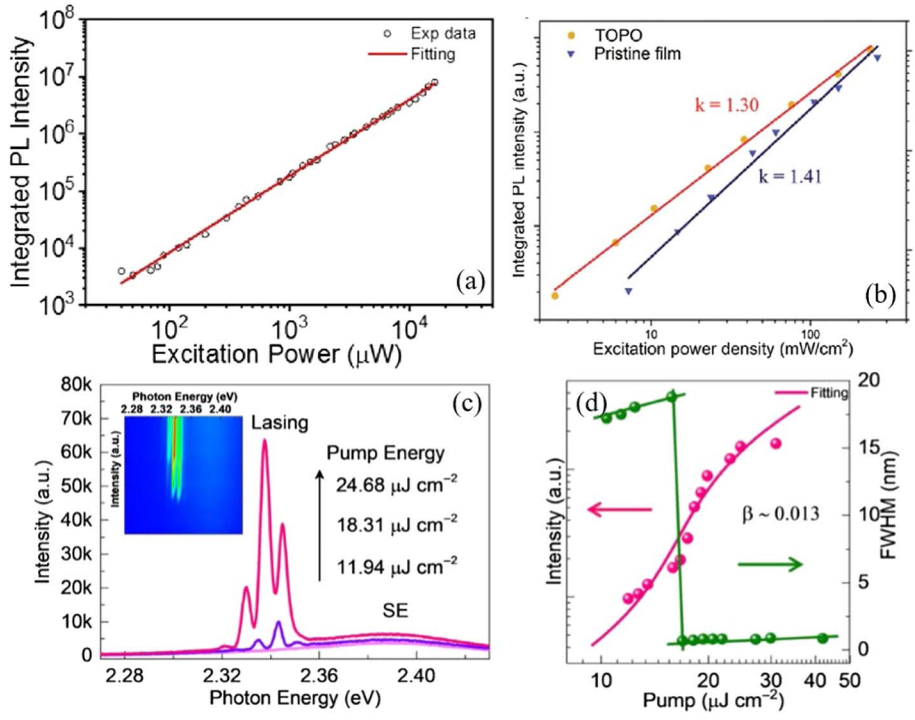

Fig. 2. (a) Integrated PL intensity linearly increasing with excitation power in $CsPbBr_3$ NCs. Reprinted with permission [27]. (b) Fitting results of excitation density dependent PL spectra of the pristine and TOPO-treated $CsPbBr_3$ perovskite films. Reprinted with permission [46]. (c) Power-dependent emission spectra indicating lasing of $CsPbBr_3$ nanowires. Inset: a two-dimensional pseudo-color plot of emission spectra at different pump fluences. (d) The power dependence of the integrated emission intensity and the FWHM of the dominant emitted lasing peak. Reprinted with permission [47].

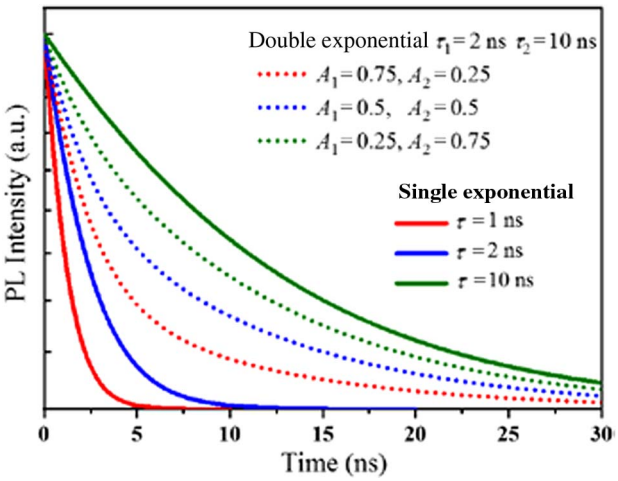

Fig. 3. Simulated TRPL curves. Solid lines were calculated by single exponential function using different lifetimes of 1 ns (red), 2 ns (blue), and 10 ns (green). Dashed curves were calculated using the double exponential formula by fixing two lifetimes of $\tau_1 = 2$ ns and $\tau_2 = 10$ ns, with a change of their weighted amplitude A.

curves for different τ values of 1, 2, and 10 ns, respectively, as shown by the three solid lines in Fig. 3, with an obvious linear dependency in the initial stage revealed by a semi-logarithmic coordinate. It can be seen from the figure that the longer the lifetime is, the slower the attenuation of the PL intensity is, implying a higher quality of bulk halide perovskite material.

Most of the reported lifetimes of all-inorganic halide perovskite materials that satisfy the single exponential relationship are in the range of 1–30 ns [49–54], as listed in Table 1. Li *et al.* investigated the effects of phase transition as well as doping (Cl) on the carrier lifetime of $CsPbBr_3$ thin films [50]. PL decay for the pure orthorhombic $CsPbBr_3$ films exhibited a time constant τ of 6.7 ns, while τ of cubic $CsPbBr_3$ film was 12.3 ns. Therefore, the phase transition of orthorhombic-to-cubic for $CsPbBr_3$ induced a significant increase in exciton lifetime. While for Cl-doped cubic $CsPbBr_3$(Cl), τ further increased to 14.3 ns, exhibiting a longer carrier lifetime. Ren *et al.* introduced the polyethylene glycol (PEG) into the precursor solution during the growth of $CsPbBr_3$ film through a one-step spin-coating process [53]. They declared that the PEG-aided perovskite thin film would have higher homogeneity since it did not induce any excessive non-radiative

Table 1. Summary of the Reported Lifetime by Single Exponential Fitting, Average Lifetime, Its Individual Lifetime and Amplitude by Double and Triple Exponential Fitting in All-Inorganic Halide Perovskites

Perovskite Material	Year	Model	τ_{ave} (ns)	τ_1 (ns)	A_1	τ_2 (ns)	A_2	τ_3 (ns)	A_3	Reference
$CsPbBr_3$ orthorhombic	2017	Single	6.7							[50]
$CsPbBr_3$ cubic			12.3							
$CsPbI_2Br$ film	2018	Single	8.6							[51]
$CsPbBr_{3-x}I_x$ QDs	2018	Single	3.57–10							[52]
$CsPbI_2Br$/Spiro-OMeTAD	2019	Single	4.6							[49]
$CsPbI_2Br/(CsPbI_2Br)_{1-x}(CsPbI_3)_x$/Spiro-OMeTAD			3.2							
$CsPbBr_3$ with PEG	2020	Single	32.1							[53]
$CsPbBr_3$ without PEG			11.8							
$CsPbI_3$	2020	Single	0.553							[54]
PEAI-$CsPbI_3$			15.358							
$CsPbI_2Br$ (GTA)	2019	Double	4.3	1.964	0.12	4.478	0.88			[55]
$CsPbI_2Br$ (GTA-AST-Tol)			6.9	1.950	0.056	7.032	0.94			
$CsPbI_2Br$ (GTA-AST-IPA)			14.1	4.806	0.12	14.516	0.88			
$CsPbI_2Br$	2019	Double	11.27	6.57	0.372	14.31	0.617			[56]
$CsPbI_2Br$	2017	Double	14	4.6	0.28	18	0.72			[57]
$Cs_{0.025}K_{0.075}PbI_2Br$			11	4	0.3	14	0.7			
$CsPbI_2Br$	2017	Double		2.2		11.1				[58]
$CsPb_{0.98}Sr_{0.02}I_2Br$				2.1		17.1				
$CsPb_{0.95}Ca_{0.05}I_3$	2018	Double	6.6	2.3		8.1				[59]
$CsPbI_2Br$	2019	Double	0.453	0.453		0.438				[60]
$CsPbI_2Br$ (0.5% Nb)			2.287	2.125		3.875				
$CsPbI_2Br$	2019	Double	2.01	2.67	0.64	1.08	0.36			[61]
$CsPbI_2Br$ (0.5% BaI_2)			16.0	11.8	0.59	22.1	0.41			
$CsPbI_2Br$	2020	Double	20.57	12.95	0.25	23.0	0.75			[62]
$CsPb_{0.98}La_{0.02}I_2Br$			48.73	10.01	0.0652	851.43	0.935			
$CsPbBr_3$ cubic	2018	Double	35.67	56.03	0.49	16.14	0.51			[63]
$CsPbBr_xI_{1-x}$ NCs	2019	Double	6.07	2.93	0.76	16.05	0.24			[64]
$CsPbBr_3$	2020	Double	13.65	3.38	0.92	27.33	0.08			[65]
$CsPbBr_3$ with IPA treatment			43.21	9.97	0.77	61.39	0.23			
$CsPbI_2Br$ NCs	2018	Triple	6.91	2.09	0.079	5.19	0.604	11.41	0.317	[66]
$CsPbBr_3$ NCs	2018	Triple	0.9	0.3	0.56	0.8	0.43	4.5	0.01	[29]
$Cs_2AgBiBr_6$ NCs	2018	Triple		0.05		1		100		[28]
$CsPbX_3$ NCs	2019	Triple	1.34–7.9							[67]
$CsPbBr_3$ NCs	2019	Triple		0.294		1.261		6.054		[27]

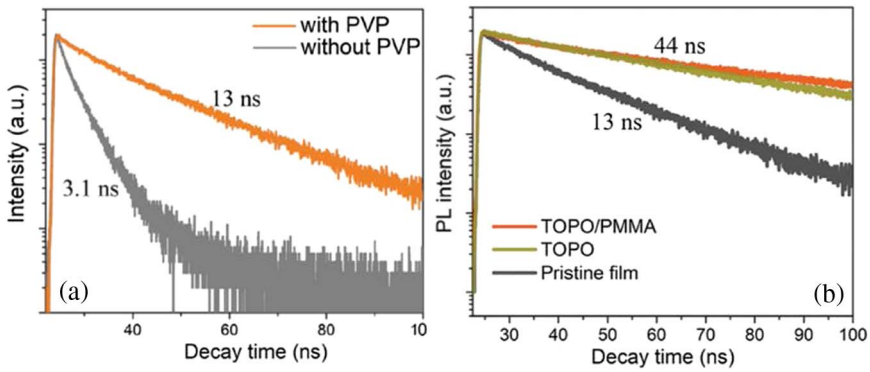

Fig. 4. (a) $CsPbBr_3$ perovskite films with and without pre-coating of PVP on the substrate and (b) pristine, TOPO-treated, and TOPO/PMMA-treated perovskite films. Reprinted with permission [46].

recombination. This deduction can be confirmed by the TRPL experiment, where the $CsPbBr_3$ film with PEG showed longer PL lifetime (32.1 ns) than that without the PEG additive (11.8 ns), indicating the beneficial influence of PEG on the thin film quality [68,69].

Jiang *et al.* investigated the effect of surface treatment on the carrier lifetime during the preparation of $CsPbBr_3$ thin film [46]. A thin layer of polyvinylpyrrolidone (PVP) was first spin-coated between the glass substrate and the $CsPbBr_3$ film [70]. The SSPL and TRPL spectra showed an obvious promotion in the PL intensity and carrier lifetime. The PL intensity was markedly improved by six times, and the carrier lifetime was prolonged from 3.1 to 13 ns, as plotted in Fig. 4(a). To find an explanation, the authors employed atomic force microscopy (AFM) images to show a roughness of 2.71 nm for the perovskite film pre-coated with PVP and 3.63 nm for that without a PVP layer, which indicated an improvement of morphology for perovskite film after the bottom treatment. Further, after introduction of passivation, an organic small molecule, TOPO, or TOPO/poly(methyl methacrylate) (PMMA) layer was introduced onto the perovskite surface to form a surface passivation layer. The PL intensity of the film increased by roughly 3 and 4 times for TOPO and TOPO/PMMA layer coating, respectively. Meanwhile, the PL decay studies [Fig. 4(b)] showed a much slower decay (44 ns) than that of the pristine film (13 ns). The authors concluded that the increase in carrier lifetime of TOPO/PMMA-treated film chiefly originated from the TOPO passivation effects, while the PL intensity improvement was ascribed to the integrated effects of TOPO and PMMA.

When $I_{PL}(t)$ and t no longer satisfy the single exponential relationship, it is necessary to use double or triple exponential fitting. For the double exponential relation, the form of $I_{PL}(t) = A_1 \exp(-\frac{t}{\tau_1}) + A_2 \exp(-\frac{t}{\tau_2}) + y_0$ is usually employed [60–77], where τ_1 and τ_2 represent the two fitted lifetime components of the decay curve, and A_1, A_2 are their weighted amplitudes. In Fig. 3, we also plotted the calculated PL decay curves using the above double exponential formula. Three different combinations of A_1 and A_2 were simulated (red short dotted curve: $A_1 = 0.75$ and $A_2 = 0.25$, blue short dotted curve: $A_1 = 0.5$ and $A_2 = 0.5$, green short dotted curve: $A_1 = 0.25$ and $A_2 = 0.75$), while the values of τ_1 and τ_2 were fixed to be 2 and 10 ns, respectively. It can be seen that the three curves were all between the two single exponential curves [$\tau = 2$ ns (blue solid curve) and $\tau = 10$ ns (green solid curve)]. With the decrease of the A_1 value, the simulated double exponential curve gradually moved away from $\tau = 2$ ns and approached the $\tau = 10$ ns single exponential curve. Therefore, we can not only extract the lifetimes of two relaxation processes, but also obtain the corresponding weight by fitting the experimental TRPL curve, which may be helpful for analyzing the different carrier dynamic processes in combination with the structural characteristics of halide perovskite materials.

The lifetimes and their weights of all-inorganic perovskite materials reported in the literature by using double exponential fitting are also listed in Table 1, as well as the calculated average lifetime τ_{ave}. It should be pointed out that two different expressions are employed to obtain this value by different research groups: one is $\tau_{ave} = A_1\tau_1 + A_2\tau_2$, while the other is $\tau_{ave} = \frac{A_1\tau_1^2 + A_2\tau_2^2}{A_1\tau_1 + A_2\tau_2}$. However, both of them are available depending on the definition of the average physical parameter. The former represents the average lifetime from the viewpoint of the number of carriers that participate in radiative recombination, while the latter represents the average lifetime of the PL intensity. We note that most of the reported compounds were quaternary or multicomponent inorganic halide perovskite films, which indicates that the inhomogeneity of structure of materials could lead to the complexity of carrier relaxation. Among them, $CsPbI_2Br$ and its based doping compounds are one kind of the most concerned materials [56,55]. For example, Chen *et al.* used a gradient thermal annealing (GTA) method to control the growth of $CsPbI_2Br$ crystals and then utilized a green anti-solvent (ATS) to further optimize the morphology of $CsPbI_2Br$ film [55]. Three samples were studied for comparison: only the GTA-treated film (named GTA), the films via GTA-ATS with toluene (Tol) as an ATS (named GTA-AST-Tol), and the films via GTA-ATS with isopropanol (IPA) as an ATS (named GTA-AST-IPA). SSPL [inset of Fig. 5(a)] showed that the intensity of the GTA-ATS-IPA film was approximately three-fold higher than that of the GTA film, indicating a dramatically decreased non-radiative recombination in the GTA-ATS-IPA film. As shown in Fig. 5(a), all three TRPL decay curves contained both the slow and fast components, where the short lifetime represented the surface

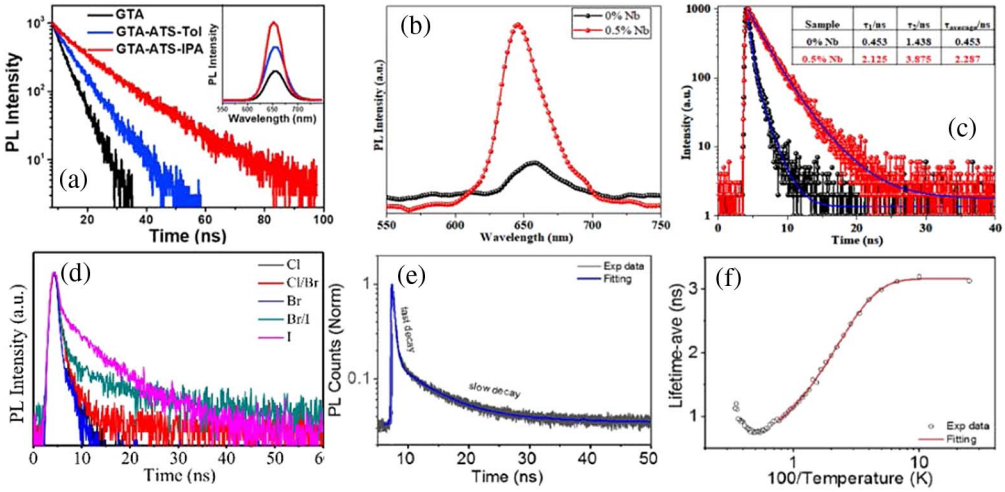

Fig. 5. (a) TRPL plots of the $CsPbI_2Br$ films fabricated on a glass substrate, treated by the GTA, GTA-ATS-Tol, and GTA-ATS-IPA processes. Inset: SSPL spectra of the corresponding $CsPbI_2Br$ films. Reprinted with permission [55]. (b) PL and (c) TRPL spectra of 0 and 0.5% Nb-doped $CsPbI_2Br$ films. Reprinted with permission [60]. (d) TRPL decay curves obtained for $CsPbX_3$ NCs with halogen ions varying from Cl to I. Reprinted with permission [67]. (e) TRPL decay profile and (f) temperature-dependent average lifetime of $CsPbBr_3$ NCs. Reprinted with permission [27].

non-radiative recombination, and the long lifetime was the bulk recombination. Both the surface and bulk recombination lifetimes of $CsPbI_2Br$ films were substantially prolonged from 1.964 and 4.478 ns to 4.806 and 14.516 ns, respectively, for the GTA and GTA-ATS-IPA films. The results revealed that the traps were reduced by the ATS treatment, especially using the IPA solvent. In addition, the weight of long lifetime was about 90%, which implied that the bulk recombination was the main path of carrier relaxation in the reported $CsPbI_2Br$ films.

More research teams have studied the carrier lifetime of doping other elements into $CsPbI_2Br$ perovskites and found that the lifetimes increased to a certain extent due to the incorporation [60–62]. The identification of the two lifetime components extracted by fitting TRPL curves using a double exponential function in the reported materials was similar; that is, the shorter lifetime corresponded to the non-radiative recombination caused by defects or surface states, and the longer lifetime referred to the intrinsic radiative recombination.

Guo *et al.* studied the effect of niobium (Nb) doping into $CsPbI_2Br$ film on the electron extraction and transport process [60]. The SSPL intensity sharply increased after 0.5% Nb incorporation, as shown in Fig. 5(b), which indicates fewer traps and defects [78]. Thus, 0.5% Nb doping can significantly reduce the traps and defects in the perovskite film, meaning a better film quality and promising better performance [79,80]. The fitted average lifetime of the carrier dynamic process [Fig. 5(c)] was also increased from 0.453 ns (reference $CsPbI_2Br$ film) to 2.287 ns (0.5% Nb-doped $CsPbI_2Br$ film). Therefore, Nb doping may suppress the recombination process in the perovskite film, which was consistent with the performances of the PSC devices [81,82]. Another barium (Ba^{2+}) alkaline earth metal cation was also proposed to be doped into $CsPbI_2Br$ perovskite [61]. Compared with the pristine $CsPbI_2Br$, the TRPL decay profile exhibited increased PL lifetime upon Ba^{2+} incorporation. Moreover, both the surface and bulk recombination lifetimes were substantially prolonged from 2.01 to 16 ns, suggesting suppression of non-radiative recombination pathways in BaI_2:$CsPbI_2Br$ perovskite thin films, which were also consistent with the improved photovoltaic performance.

Another common type of doping is the substitution of Pb atoms in $CsPbI_2Br$ to form five element perovskite materials. Lau *et al.* incorporated the less toxic strontium (Sr^{2+}) at a low concentration that partially substituted Pb in $CsPb_{1-x}Sr_xI_2Br$ with x changing from 0 to 0.05 [58]. The fitted defect trapping lifetime (fast component) of all the films was relatively the same, with a value of 2 ns. However, as the Sr content increased from 1% to 2%, the effective recombination lifetime (slow component) increased from 11.1 to 17.1 ns, suggesting a better effective recombination lifetime. This suggests better surface passivation provided by the Sr enriched surface. However, as the Sr content increased further, the excess Sr^{2+} doping in the perovskite film enhanced electron–hole recombination. Similar halide perovskite compounds formed by lanthanum (La^{3+}) substitution doping were $CsPb_{1-x}La_xI_2Br$, reported by Chen *et al.* recently [62]. Through fitting the PL decay curves, the average carrier lifetimes for $CsPbI_2Br$ and $CsPb_{0.98}La_{0.02}I_2Br$ were calculated to be 20.57 and 48.73 ns, respectively. The carrier lifetime at 2% La^{3+} doping was twice that of the pristine thin film, indicating that the film defects were greatly passivated after La^{3+} doping, which reduced the non-radiative recombination. However, similar to the case of Sr doping as discussed above, by further increasing the La^{3+} doping concentration to 3%, the carrier lifetime was sharply reduced, which may be due to the introduction of defects by excess La^{3+} ions.

For the more complex relaxation processes, it is necessary to use the three exponential relationship to better fit the TRPL curve: $I_{PL}(t) = A_1 \exp(-\frac{t}{\tau_1}) + A_2 \exp(-\frac{t}{\tau_2}) + A_3 \exp(-\frac{t}{\tau_3}) + y_0$, where τ_1, τ_2, and τ_3 represent the three fitted lifetime

components, and A_1, A_2, and A_3 are their corresponding weighted amplitudes. The average lifetime is calculated by the formula $\tau_{ave} = A_1\tau_1 + A_2\tau_2 + A_3\tau_3$ or $\tau_{ave} = \frac{A_1\tau_1^2 + A_2\tau_2^2 + A_3\tau_3^2}{A_1\tau_1 + A_2\tau_2 + A_3\tau_3}$. Table 1 also lists the reported samples that used three exponential fitting. It is interesting to find that most of these perovskites were nanostructured materials [27–29,67,83]. Chen *et al.* studied the TRPL decay curves [Fig. 5(d)] of $CsPbX_3$ (X = Cl, Br, I, Cl/Br, and Br/I) NCs by three exponential components, containing types of defect emissions in doping and surface defect emission [83]. The obtained average lifetimes were in the range from 1.34 ns ($CsPbBr_3$) to 7.9 ns ($CsPbI_3$). It was argued that the average lifetime was related to the size of the NCs. The larger size of NCs decreased the probability of carriers approaching the surface, leading to the lower non-radiative recombination rate and higher PLQY (about 70%) due to the enhanced radiation process.

Shi *et al.* investigated the TRPL decay curves of $CsPbBr_3$ NCs deeply [27]. The curve could be globally fitted smoothly with a short time ($\tau_1 = 0.294$ ns), an intermediate time ($\tau_2 = 1.261$ ns), and a long time ($\tau_3 = 6.054$ ns) with different amplitudes, as shown in Fig. 5(e). The short lifetime of 0.294 ns corresponded to the direct recombination of excitons in the material, which contributed to the PL fast decay in colloidal $CsPbBr_3$ NCs, while the intermediate (long) time constant corresponded to the photo-excited electrons (holes) path along trapping–detrapping recombination with holes (electrons), contributing to the PL slow decay. The above deduction was further confirmed by the thermal effect, which could increase the TS and reduce the detrapping effect, changing the occupied percentage of indirect and direct recombination for excitons. As plotted in Fig. 5(f), the exciton mainly underwent indirect recombination at low temperature, balanced at the temperature of 130–150 K, and direct recombination at high temperature.

We noticed that either the photo-generated carriers or excitons have been mentioned by different groups in all-inorganic halide perovskites. However, the coexistence of free carriers and excitons as well as typical excitonic effects such as exciton resonance [84], exciton localization [85], and exciton polaritons [86] may be the potential situation. In the case of the coexistence of carriers and excitons, the exponential relationship may not be available, and some other theories have been proposed. For example, a stretched exponential formula $I_{PL}(t) = e^{-(\frac{t}{\tau})^{\beta}}$ was employed to calculate the lifetime of orthorhombic $CsPbI_3$, and the fitting values of τ and β were 50 ns and 0.66 [87]. Another reported fitting model is the thermalized stretching exponential line [88–90]:

$$I_{PL}(t) = A_1 e^{(-\frac{t}{\tau_1})} + A_2 e^{-(\frac{t}{\tau_2})^{\beta}}. \quad (1)$$

The above model is regarded as evidence of the exciton localization, in which the parameter β is related to the dimensionality of the localizing canters. The former exponential term in Eq. (1) represents the relaxation of free or extended states towards localized states, whereas the latter stretched exponential term accounts for the communication between the localized states. A_1, A_2 and τ_1, τ_2 are the corresponding weight fractions and decay times for free and localized excitons. Dey *et al.* used this theory to study the dynamic process of $CsPbBr_3$ NC film, and the extracted values of τ_1 and τ_2 at 300 K were 3.64 and 8.16 ns, respectively [91]. When the temperature decreased from 300 to 10 K, the free exciton lifetime decreased first and then increased, while the local exciton lifetime monotonically decreased. Further, the value of β is higher (≈0.72) at 300 K and then reduced to ≈0.57 at 10 K, which reflected the distribution of traps and the corresponding trapped exciton release rates.

Changing the incident excitation energy can not only affect the SSPL as discussed above, but it also affects the TRPL spectrum, especially the PL intensity just after photoexcitation. However, the former focuses on the discussion of the recombination mechanism, while the latter is generally a good indicator of the nature of the radiative recombination processes [92]. In short, the initial PL intensity ($t = 0$) is mainly linear with the photoexcitation density n for the exciton recombination and proportional to n^2 for free carrier recombination, respectively [93–95].

Ning *et al.* investigated the radiative recombination mechanism of the double halide perovskite $Cs_2AgBiBr_6$ film [71]. When the carrier density was between 10^{16} and 10^{17} cm^{-3}, the PL intensity showed power dependence on the carrier density with a scaling factor (λ) of 1.34 [Fig. 6(a)]. This value suggested either the coexistence of radiative recombination of the free electrons–holes and the free carriers with doped carriers or

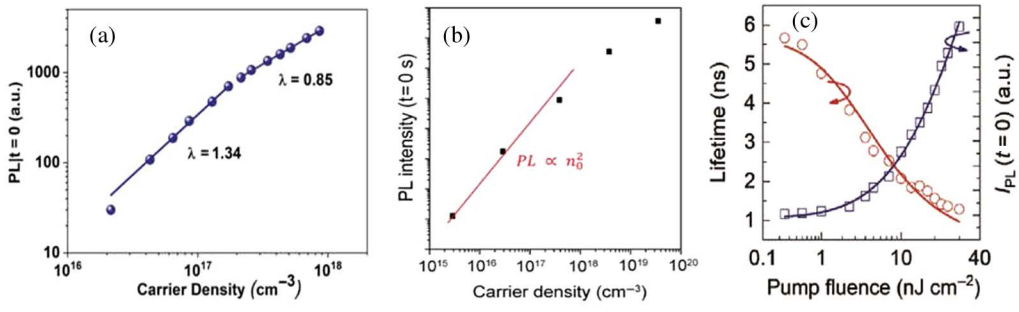

Fig. 6. (a) PL intensity just after photoexcitation as a function of carrier density of $Cs_2AgBiBr_6$ double halide perovskite film. Reprinted with permission [71]. (b) Initial PL intensity after laser excitation as a function of injected carrier density with the quadratic dependence at lower injected carrier density in the range of ~10^{15}–10^{17} cm^{-3} (solid red line) of $CsPbI_3$ halide perovskite film. Reprinted with permission [87]. (c) Lifetime and $I_{PL}|_{t=0}$ versus pump fluence in $CsPbBr_3$ nanowires. Reprinted with permission [96].

the coexistence of excitons and free electrons–holes in the measured excitation density range. Further increasing the carrier density to above 10^{17} cm^{-3} caused the λ to decrease to 0.85, implying strong high-order recombination such as exciton–carrier and exciton–exciton Auger recombination at high carrier densities.

Fu *et al.* studied the initial PL intensity just after excitation as a function of carrier density of the $CsPbI_3$ perovskite film [87]. As shown in Fig. 6(b), PL intensity increased quadratically with carrier density from 2.8×10^{15} to 3.9×10^{17} cm^{-3} and then approached saturation at higher carrier densities. It is considered that at low density, this quadratic dependence revealed that the photo-excited carriers were mainly free carriers, and the emission was dominated by free carrier bi-molecular recombination. As the density increased ($>10^{18}$ cm^{-3}), a higher-order recombination channel (i.e., Auger recombination) may appear. A similar phenomenon was also observed in the relationship between PLQY and incident carrier density of the concerned samples.

To confirm the origin of the recombination process in $CsPbBr_3$ nanowires, Li *et al.* extracted out the power-dependent PL lifetime and initial intensity $I_{PL}(t = 0)$, as shown in Fig. 6(c) [96]. By increasing the incident pump fluence, the PL lifetime decreases, while the $I_{PL}(t = 0)$ is nearly linear with the excitation density. These results suggest that free carrier recombination is the main source of emission under the current excitation condition. The author also noted that the $CsPbBr_3$ binding energy (≈40 meV) is higher than the thermal energy at room temperature; however, they speculated that the high-power laser excitation may induce an increase to the local temperature and lead to exciton dissociation.

C. Temperature Effect on PL

The temperature dependency of PL spectra gives useful information about the physical properties in all-inorganic halide perovskites such as exciton binding energy, longitudinal optical (LO) phonon energy, exciton–phonon coupling strength, and the density of defects. Among them, the exciton binding energy and the exciton–phonon coupling strength are key parameters to clarify the nature of photo-generated charges, that is, free carriers or excitons. This will help interpret the counterintuitive fact that perovskites can act both as extraordinary photovoltaic materials and superior gain media for lasing. In general, photovoltaic materials require efficient separation of photocarriers, while lasing materials require high recombination rates [97,98].

Figure 7(a) shows typical temperature-dependent PL spectra of $CsPbBr_3$ nanowires [96]. It is obvious that the PL position as well as the FWHM of the luminescence peak changes with the temperature. With increasing temperature, the emission peak exhibits blue shift (indicated as black arrow), suggesting an increasing bandgap. The temperature dependency of the FWHM is plotted in Fig. 7(b), and, clearly, the FWHM increases by increasing the temperature. Further, temperature-dependent PL can be used to probe the density of defects and exciton–phonon coupling by fitting the following expression [99]:

$$\Gamma(T) = \Gamma_0 + \sigma T + \frac{\Gamma_{LO}}{e^{\frac{\hbar\omega_{LO}}{k_B T}} - 1}, \tag{2}$$

where the first term Γ_0 is the inhomogeneous line width. The second term σ represents the exciton-acoustic phonon coupling coefficient. The third term represents the homogeneous broadening term, which originates from the scattering with the LO phonons. Γ_{LO} and $\hbar\omega_{LO}$ represent the exciton–optical phonon coupling coefficient, and LO phonon energy, respectively.

The extracted parameters of the studied $CsPbBr_3$ nanowires are also listed in Fig. 7(b), where the inhomogeneous line width Γ_0 is 14.13 meV, arising from the scatterings with disorder and imperfections, and the exciton–LO phonon coupling coefficient is about 88.45 meV. Moreover, the authors mentioned that the obtained data are smaller than the previous reported values for $CsPbBr_3$ nanowires with different widths [47], which may be caused by the effect of lattice distortion.

Similar investigations were carried out in $CsPbBr_3$ microsphere cavities for lasing applications [100]. It is found that phonons of different energies are dominant at different temperature regions, as shown in Fig. 7(c) with the fitted parameters correspondingly. Besides, the exciton–phonon coupling strength Γ_{LO} in region II is much stronger than that in region I. Thus, the authors conjectured that two different phonon modes participated in the exciton–phonon scattering, and the LO energy of 15.3 meV is more significant.

The exciton binding energy can be simulated by fitting the temperature dependency of the PL intensity of the SSPL spectra using an Arrhenius equation [101,102]:

$$I(T) = \frac{I_0}{1 + Ae^{-\frac{E_B}{k_B T}}}, \tag{3}$$

where I_0 is the intensity at 0 K, E_B is the exciton binding energy, which is also related to the thermal activation energy if no other exciton decay channel exists [103,104], and k_B is the Boltzmann constant.

For inorganic perovskites, the temperature effect in $CsPbX_3$ nanomaterials was relatively widely studied [91,103–110], and most of the applied temperature range was 80–300 K. However, a very low temperature (below 10 K) [91,105,106] or higher temperature (up to 380 K) [104,107,109] was also investigated. The calculated exciton binding energies from the above research groups are listed in Table 2. It is found that most of the energy is larger than thermal energy of about 25.9 meV at room temperature (300 K), which means that the excitons in $CsPbX_3$ nanoscale materials should be very stable at room temperature.

Some research groups also compared the values of exciton binding energies under distinct growth conditions as well as experimental parameters. Shinde *et al.* studied the SSPL for three different-sized $CsPbBr_3$ quantum dots (QDs) in a temperature range between 10 and 300 K [106]. The exciton binding energies decrease with increasing QD size from 50 to 35 meV as a manifestation of quantum confinement. Similar results have been found in $CsPbBr_3$ nanowires with two different thicknesses of 15 and 250 nm, and the exciton binding energies are evaluated as 93 and 65 meV, respectively [111]. The higher value in the thinner nanowires could be attributed to the relatively larger wavefunction overlap between electrons [112].

Yuan *et al.* have analyzed the relationship between exciton binding energy and annealing temperature during the growth of $CsPbBr_3$ NCs [109]. It is found that with the increasing annealing temperature from 300 to 400 K, the binding energy value decreases from 63.9 to 44.1 meV, which suggests that new non-radiative recombination centers were gradually brought into the NCs with the increasing thermal annealing temperature. Actually, changing the annealing temperature may lead to the variation of NC size, which causes the different exciton binding energies.

It should be noted that the extraction of exciton binding energy from temperature-dependent PL is an indirect way, which is subject to some doubts. Thus, other techniques were proposed, and, for example, a magneto-optical study, by which the exciton binding energy can be measured directly, was performed recently [113]. In their work, the large exciton binding energy of $CsPbCl_3$ compounds was measured, which made them very promising materials for opto-electronic and polaritonic applications at room temperature.

The dependency of carrier lifetime on temperature can be obtained by the analysis of PL decay measured at varying temperatures. Wei *et al.* studied the TRPL curves of $CsPbBr_3$ QDs in a wide temperature range from 80 to 380 K [Fig. 7(d)] [107]. As shown in the inset of Fig. 7(d), the lifetime increased monotonically below room temperature and revealed a maximum (2.4 ns) at ~300 K. With further increasing temperature, the lifetime was reduced. This observation was caused by the effect of competition between non-radiative and radiative recombinations. Similar phenomena were reported by Li *et al.* [104], where temperature dependency of SSPL was carried out

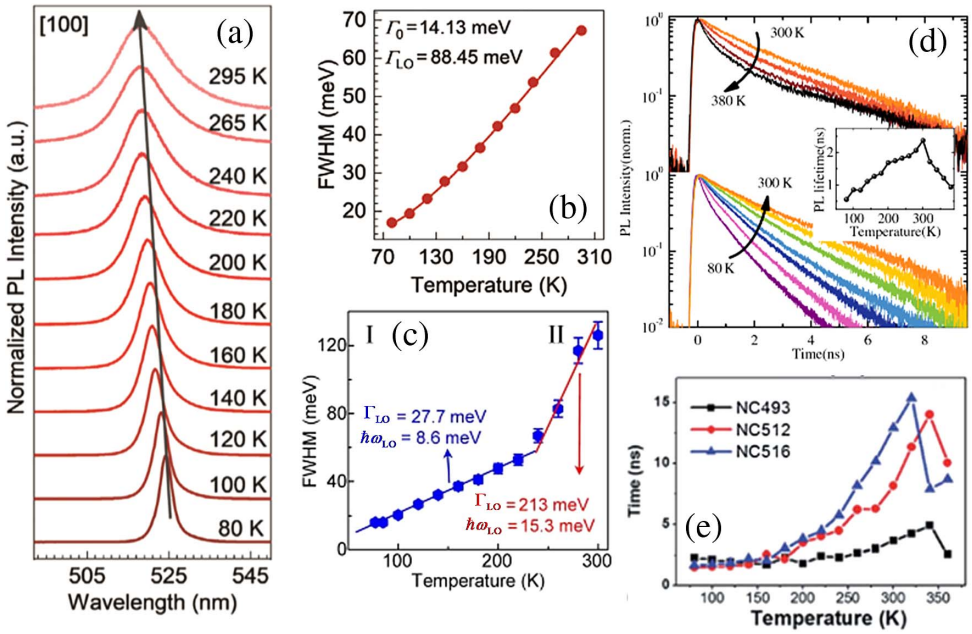

Fig. 7. (a) Temperature-dependent PL spectra for $CsPbBr_3$ nanowires within the range of 80–295 K. The emission peak shows an evident blue shift (black arrow) and broadening with increasing temperature. (b) Temperature dependence of the FWHM extracted out from (a). Reprinted with permission [96]. (c) FWHM as a function of temperature of $CsPbBr_3$ sphere. Reprinted with permission [100]. (d) Temperature-dependent PL decay curves of colloidal $CsPbBr_3$ QDs with the temperature ranging from 80 to 380 K. (e) Average PL lifetimes of $CsPbBr_3$ NCs for NC493, NC512, and NC516 samples at various temperatures. Reprinted with permission [104].

Table 2. Summary of the Exciton Binding Energy by Arrhenius Equation in $CsPbX_3$ Low-Dimensional Materials

Perovskite Material	Year	Exciton Binding Energy (meV)	Reference
$CsPbBr_3$ 15 nm thick nanowires	2018	93	[111]
$CsPbBr_3$ 250 nm thick nanowires		65	
$CsPbBr_3$ QDs with 5.5 nm size	2017	50	[106]
$CsPbBr_3$ QDs with 7.3 nm size		48	
$CsPbBr_3$ QDs with 10.1 nm size		34	
$CsPbBr_3$ QDs	2017	15.6	[103]
$CsPb(Br/I)_3$ QDs		28.2	
$CsPbI_3$ QDs		45.1	
$CsPbClBr_2$ NCs	2018	68.1	[108]
$CsPbBr_3$ NCs		62.7	
$CsPbBrI_2$ NCs		54.6	
$CsPbBr_3$ NCs	2016	35	[104]
$CsPbBr_3$ NCs annealed at 300, 320, 340, 360, 380, 400 K	2017	63.9, 61.4, 53.6, 51.8, 49.4, 44.1 correspondingly	[109]

in $CsPbBr_3$ NCs with emissions at 493 nm (NC493), 512 nm (NC512), and 516 nm (NC516), respectively. The obtained average PL lifetimes of the NCs increased with increasing temperature between 320 and 340 K and then significantly decreased, as shown in Fig. 7(e). The reduced PL lifetimes of NC samples with increasing temperature above 320 K might result from the thermal degradation of the NCs because of the loss of ligands on the surface of NCs or formation of nonradiative recombination centers, which did not occur at low temperatures [114].

4. PEROVSKITE FILM WITH TRANSPORT LAYER

A. Photo-Induced Carrier Extraction Effect

One of the most common applications of halide perovskites is the photovoltaic effect. Photo-generated carriers need to be separated rapidly in the materials and transported to their respective electrodes. This process takes less time than radiative recombination. Therefore, since the total amount of generated carriers remains unchanged, the carriers in bulk materials decrease rapidly due to their participation in transport, leading to the significantly weakened SSPL intensity, which is also known as quenching. To enhance the effect of carrier separation and transportation, an electron TL (ETL) [50,63,57,115,116] or a hole TL (HTL) [49,117–120] is usually added to the perovskite film to act as a quencher layer. The observed TRPL curve of the film with ETL (or HTL) will be steeper than that of the pristine sample due to the rapid reduction of carriers remaining in the bulk material, and the carrier relaxation lifetime obtained by fitting will be reduced correspondingly. It should be noted that for perovskite thin film (or bulk) samples, the gentler the TRPL curve is revealed, the better performance the material has, while the situation may be completely different in the samples with ETL (or HTL). The above argument makes clear that SSPL and TRPL curves are also useful characterizations that can be employed to investigate the effect of the TL on perovskite materials. Table 3 lists the reported lifetimes fitted from TRPL curves that are pristine and with ETL (or HTL) samples, respectively.

1. $CsPbX_3$

Li *et al.* studied the quenching effect of TiO_2 as ETL in cubic $CsPbBr_3$, orthorhombic $CsPbBr_3$, and cubic $CsPbBr_3$(Cl), respectively [50]. For the orthorhombic $CsPbBr_3$, the τ reduced from 6.7 to 3.9 ns. Notably, for cubic $CsPbBr_3$, the τ decreased more significantly from 12.3 to 1.8 ns, and, for the cubic $CsPbBr_3$(Cl), the value was from 14.3 to 1.5 ns, which is in good agreement with the results of SSPL observation. Thus, it can be concluded that the electron extraction was more effective by TiO_2 ETL at the $CsPbBr_3$(Cl)/TiO_2 interface due to the effect of Cl doping. To optimize the effect of the ETL, Liu *et al.* analyzed the PL spectra of $CsPbBr_3$, TiO_2/$CsPbBr_3$, and TiO_2/SnO_2/$CsPbBr_3$ samples deposited on fluorine-doped tin oxide (FTO) substrates [63]. As shown in Fig. 8(a), obvious SSPL quenching was observed when the TiO_2 and TiO_2/SnO_2 ETLs were introduced. The TiO_2/SnO_2/$CsPbBr_3$ sample also showed a stronger PL-quenching efficiency than the TiO_2/$CsPbBr_3$ sample, suggesting a more efficient electron–hole separation and lower carrier recombination at the bilayered ETL/perovskite interface.

Table 3. Summary of the Reported Lifetime with and without Quencher Layer in All-Inorganic Halide Perovskites, Together with the Calculated Transfer Efficiency

Perovskite Material	Year	Lifetime without TL (ns)	Quencher Layer (Type)	Lifetime with TL (ns)	Efficiency (%)	Reference
$CsPbBr_3$ orthorhombic	2017	6.7	TiO_2 (ETL)	3.9	41.79	[50]
$CsPbBr_3$ cubic		12.3	TiO_2 (ETL)	1.8	85.37	
$CsPbBr_3$(Cl) cubic		14.3	TiO_2 (ETL)	1.5	89.51	
$CsPbBr_3$	2018	35.67	TiO_2 (ETL)	5.47	84.66	[63]
			TiO_2/SnO_2 (ETL)	2.2	93.83	
$CsPbBr_3$	2019	17.16	MnS (HTL)	7.58	55.83	[121]
$CsPbBr_3$	2019	0.88	$CsPbBr_3$ NCs (HTL)	0.45	48.86	[122]
			$CsPbBr_2I$ NCs (HTL)	0.3	65.91	
			$CsPbBrI_2$ NCs (HTL)	0.51	41.05	
			$CsPbI_3$ NCs (HTL)	0.16	81.82	
$CsPbI_3$	2017	50	$PC_{61}BM$ (HTL)	7.2	85.60	[87]
			Spiro-OMeTAD (ETL)	0.8	98.40	
$CsPbI_2Br$	2018	1.45	C_{60} (ETL)	1.04	28.28	[123]
			ZnO (ETL)	1.43	1.38	
			ZnO@C_{60} (ETL)	0.73	49.66	
$CsPbI_2Br$	2018	8.6	SnO_2 (ETL)	2.9	66.28	[51]
			SnO_2/ZnO (ETL)	1.2	86.05	
$CsPbI_2Br$	2019	2.12	SnO_2 (ETL)	1.27	42.53	[124]
$CsPbI_2Br$	2019	22.65	Spiro-OMeTAD (HTL)	9.59	56.92	[117]
			2mF-X59 (HTL)	6.63	70.22	
			2mF-X59 + F4-TCNQ (HTL)	4.71	79.21	
$CsPbI_2Br$	2019	4.5	Bi_2Te_3 interlayer (HTL)	2.21	50.89	[125]
$CsPbI_2Br$	2020	1.45	N749 interlayer (HTL)	0.75	48.28	[118]
$Cs_2AgBiBr_6$	2018	13.7	$PC_{61}BM$ (ETL)	2.4	82.48	[71]
			Spiro-OMeTAD (HTL)	2.6	81.02	

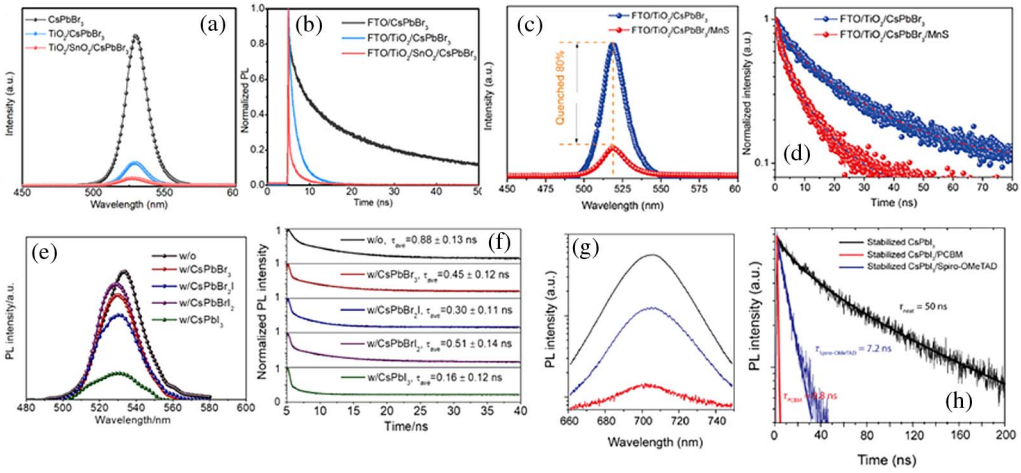

Fig. 8. (a) SSPL and (b) TRPL spectra of the $CsPbBr_3$ films deposited on FTO, TiO_2, and TiO_2/SnO_2 ETLs. Reprinted with permission [63]. (c) SSPL and (d) TRPL spectra of the $CsPbBr_3$ perovskite films with and without MnS HTL. Reprinted with permission [121]. (e) SSPL and (f) TRPL spectra of FTO/c–TiO_2/m–TiO_2/$CsPbBr_3$ covered with and without $CsPbBr_xI_{3-x}$ NCs. Reprinted with permission [122]. (g) SSPL and (h) TRPL spectra of the neat $CsPbI_3$ (black curve), $CsPbI_3/PC_{61}BM$ (blue curve), and $CsPbI_3$/Spiro–OMeTAD (red curve) films. Reprinted with permission [87].

The corresponding TRPL decay curves of the same samples are plotted in Fig. 8(b). The average carrier lifetime of $TiO_2/CsPbBr_3$ sample dropped from 35.67 to 5.47 ns and further decreased to 2.20 ns for the $TiO_2/SnO_2/CsPbBr_3$ sample, which is in good agreement with the SSPL observation.

To study the HTL effect on $CsPbBr_3$, Li *et al.* introduced MnS with the intermediate energy levels as HTL at the interface of $CsPbBr_3$/carbon [121]. As illustrated in Fig. 8(c), the $CsPbBr_3$ film covered with MnS showed a lower PL intensity than the $CsPbBr_3$ without any intermediate layer, indicating a stronger hole extraction capability at the interface between perovskite and MnS HTL. Moreover, compared to 17.16 ns lifetime for the pristine sample, a shorter carrier decay lifetime of 7.58 ns with MnS layer [Fig. 8(d)] also confirmed the enhanced hole transfer and suppressed interface recombination between the perovskite layer and carbon [126,127]. Su *et al.* employed $CsPbBr_xI_{3-x}$NCs as the HTL layer in carbon-based all-inorganic $CsPbBr_3$ PSCs [122]. Figure 8(e) shows the SSPL spectra of all the samples. In contrast to high-intensity PL peaks of pristine $CsPbBr_3$ films, PL intensities of $CsPbBr_xI_{3-x}$ tailored $CsPbBr_3$ films were lower on account of quenching effects, indicating efficient photo-induced electron–hole separation and low carrier recombination. The TRPL curves of the pristine $CsPbBr_3$ film and those four with $CsPbBr_xI_{3-x}$ NC HTL samples were measured, as shown in Fig. 8(f), together with the calculated carrier average lifetime of each sample. The decrease of average lifetime in $CsPbBr_xI_{3-x}$ NCs tailored $CsPbBr_3$ films verified the elimination of non-radiative paths and the enhancement of hole separation and transfer.

Charge transport properties of the stabilized $CsPbI_3$ thin film were explored by spin-coating an ETL of [6,6]-phenyl C_{61} butyric acid methyl ester ($PC_{61}BM$) or an HTL of 2,2′,7,7′-tetrakis-(N, N– di-4-methoxyphenylamino)-9, 9′-spirobifluorene (Spiro-OMeTAD) [87]. Figure 8(g) shows the SSPL intensities of three samples: neat $CsPbI_3$, $CsPbI_3/PC_{61}BM$, and $CsPbI_3$/Spiro-OMeTAD. The intensities were significantly quenched in films coated with TLs compared to that of the neat film. The TRPL curves of the three samples are plotted in Fig. 8(h), and the obtained average lifetimes reduced from 50 to 7.2 ns (with Spiro-OMeTAD HTL) and 0.8 ns (with $PC_{61}BM$ ETL), which means a better transfer effect in film with ETL than that with HTL.

2. $CsPbI_2Br$

More research was focused on the ETL (or HTL) effect on $CsPbI_2Br$ perovskite, where optimized TL structures were proposed to achieve better carrier transportation [128]. Liu *et al.* proposed a novel structure with ZnO@C_{60} as an ETL [123]. Compared with the single ZnO-based or C_{60}-based sample, PL quenching in the ZnO@C_{60}-based sample was faster [shown in Fig. 9(a)], exhibiting higher electron extraction efficiency. Aside from the reduced TS density, the authors assumed it was likely attributed to the good gradient energy band matching between the perovskite layer and ZnO@C_{60} bilayer, which favored the photo-generated electrons to be extracted from the perovskite layer to the metal electrode effectively. Zhou *et al.* [124] and Yan *et al.* [51] investigated a similar structure of ITO/SnO_2/ZnO/$CsPbI_2Br$/Spiro–OMeTAD/MoO_3/Ag. The former studied the effect of the SnO_2 layer, and the latter focused on the effect of SnO_2 as well as the SnO_2/ZnO bilayer. By analyzing the extracted carrier lifetime from TRPL curves, as plotted in Figs. 9(b) and 9(c), both SnO_2 and SnO_2/ZnO layers revealed the role of enhancing the carrier transport. The highly efficient charge extraction and suppressed interfacial trap-assisted recombination were due to the existence of desirable cascade energy level alignment between perovskite and the designed ETL structure.

Other research groups focused on the effect of the HTL structure in $CsPbI_2Br$. For example, N′, N′, N″, N″-tetrakis (4-methoxyphenyl)spiro[fluorene-9, 9′-xanthene]-2,7-diamine (2mF-X59) plus 2,3,5,6-tetrafluoro-7,7,8,8-tetracyanoquinodimethane (F4-TCNQ) was employed as an HTL [117]. SSPL spectra revealed that ~92% emission was quenched

for the perovskite film coated with 2mF-X59 + F4-TCNQ, which is higher than that of the perovskite films with 2mF-X59 (73%) and Spiro-OMeTAD (54%), as shown in Fig. 9(d). TRPL decay [Fig. 9(e)] was fitted by a double exponential function, with the fitted $\tau_{ave} = 22.65$ ns for the bare perovskite, $\tau_{ave} = 9.59$ ns for the perovskite/Spiro-OMeTAD film, $\tau_{ave} = 6.63$ ns for the perovskite/2mF-X59 film, and $\tau_{ave} = 4.71$ ns for the perovskite/2mF-X59 + F4-TCNQ film, respectively. Obviously, the perovskite film with 2mF-X59 + F4-TCNQ showed the shortest lifetime compared to other films, indicating that the 2mF-X59 + F4-TCNQ can not only significantly inhibit trap-induced non-radiative recombination but also efficiently extract the hole. Fu *et al.* designed bismuth telluride (Bi_2Te_3, BT) nanoplates as an interlayer between $CsPbI_2Br$ and Spiro-OMeTAD [125]. As shown in the inset of Fig. 9(f), a remarkable SSPL quenching of $Bi_2Te_3/CsPbI_2Br$ film was observed, together with the sharp reduction of carrier lifetime fitted based on TRPL compared with the pristine film [Fig. 9(f)], confirming that the Bi_2Te_3 layer can significantly suppress radiative recombination and is capable of facile hole extraction from $CsPbI_2Br$ film.

3. Perovskite with Other Interfaces

PL quenching can also be observed in perovskites with other interfaces instead of traditional TLs [129–131]. Figure 9(g) plots the PL spectra of $CsPbBr_3$ microplatelet single crystals on GaN and mica substrates, respectively [131]. Quantitative studies demonstrate that the PL intensity of the $CsPbBr_3$ on the GaN substrate is ~7.2% of that on mica, suggesting that the PL quenching is not due to the difference in sample crystallinity but the interface structure. Carrier dynamics are further studied by excitation-density-dependent TRPL. The TRPL curves of $CsPbBr_3$–mica are well fitted by a single exponential decay function [Fig. 9(h)], while $CsPbBr_3$–GaN contains two decay channels [Fig. 9(i)]. The slow decay channel, with a longer lifetime, corresponds to the radiative recombination of free carriers that are not influenced by the $CsPbBr_3$/GaN interface. However, the fast decay channel, with a shorter lifetime, is attributed to the loss of carriers at the interface due to charge extraction or interface recombination.

4. Transfer Efficiencies

From the data summarized in Table 3, it can be seen that the carrier lifetime obtained by TRPL with ETL (or HTL) is smaller than that without TLs, and the smaller the value is, the better the electron (hole) transfer effect will be. In order to more quantitatively characterize the effect of the TLs, Xing *et al.* introduced the concept of transfer efficiency ϕ, by using the formula [95]

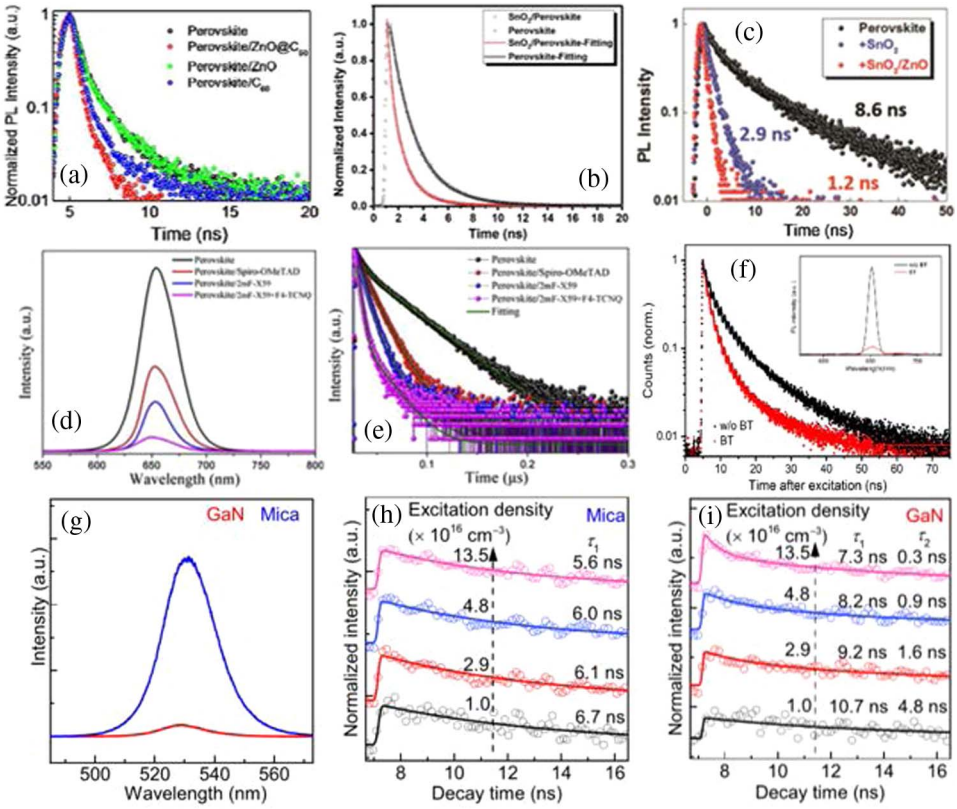

Fig. 9. (a) TRPL spectra of $CsPbI_2Br$ thin films based on different ETLs. Reprinted with permission [123]. (b) TRPL spectra of $CsPbI_2Br$ thin films with and without SnO_2 ETL. Reprinted with permission [124]. (c) TRPL decay profiles for $CsPbI_2Br$, $SnO_2/CsPbI_2Br$, and $SnO_2/ZnO/CsPbI_2Br$. Reprinted with permission [51]. (d) SSPL and (e) TRPL spectra of $CsPbI_2Br$ perovskite and $CsPbI_2Br$ perovskite covered with different HTLs. Reprinted with permission [117]. (f) TRPL and SSPL (inset) spectra of the $Bi_2Te_3/CsPbI_2Br$ films. Reprinted with permission [125]. (g) PL spectra of $CsPbBr_3$ microplatelet single crystals on GaN/mica. Power-dependent TRPL spectra of $CsPbBr_3$ on (h) mica and (i) GaN. Reprinted with permission [131].

$$\frac{1}{\tau_{\text{Heterojunction}}} = \frac{1}{\tau_{\text{Perovskite}}} + \frac{1}{\tau_{\text{CT}}}, \tag{4}$$

where $\tau_{\text{Heterojunction}}$ is the lifetime with ETL (or HTL), and $\tau_{\text{Perovskite}}$ is the lifetime of the bare film. After calculating the charge carrier transfer time τ_{CT}, the transfer efficiency can be estimated by the relation

$$\phi = \frac{\tau_{\text{Heterojunction}}}{\tau_{\text{CT}}}. \tag{5}$$

The electron (hole) transfer efficiencies ϕ of recently reported all-inorganic halide perovskite materials with ETL (or HTL) were calculated and listed in Table 3. Most of the values can exceed 50%, and some of them are as high as 90%. Especially for the research of optimizing the TL structure, the obtained ϕ of the perovskite samples with newer TL can usually be increased by 20%–30% [117,122,123]. Generally speaking, the perovskite samples grown with TL were usually used for the application of PSCs, and thus, one may argue that there is a positive relationship between ϕ and the PSC efficiency. However, after carefully analyzing the reported data of all-inorganic halide perovskite materials, no direct correlation was found between them. Nevertheless, the reasons may need to be further explored, which is beyond the scope of this article and will not be discussed here.

B. Other Transport Parameters

Diffusion coefficient D, diffusion length L_D, as well as mobility μ are also important parameters to characterize the transport ability of carriers in halide perovskite materials. The larger the diffusion length is, the longer distance the photo-generated carriers can move before recombination, which are more likely to form a photocurrent. The diffusion length of more than 1 mm was first observed in hybrid halide perovskite films of mixed halide ($CH_3NH_3PbI_{3-x}Cl_x$) [132] and triiodide ($CH_3NH_3PbI_3$) [95], which is consistent with far superior performance in planar heterojunction PSCs. After that, many research groups also paid attention to the transport properties, i.e., diffusion coefficient and length, of all-inorganic halide perovskites by further analyzing the experimental TRPL curves quantitatively.

Since the instantaneous PL intensity is directly related to the instantaneous carrier concentration n, and, if we can get the change of carrier density with time, the PL decay dynamics can be simulated accordingly. The number and distribution of carrier density in the film $n(x,t)$ satisfy the one-dimensional diffusion equation [94,132]

$$\frac{\partial n(x,t)}{\partial t} = D\frac{\partial^2 n(x,t)}{\partial x^2} - k(t)n(x,t), \tag{6}$$

where $k(t)$ is the PL decay rate of material without the TLs, and $n(x,t)$ is the spatial charge carrier density. Because the samples were photo-excited from the glass substrate side, the initial distribution of photoexcitation was given by $n(x,0) = n_0 \exp(-\alpha x)$, where α is the absorption coefficient. In the quenching experiments, it is assumed that all the photo-excited carriers that reach the interface will be quenched, which yields $n(l,t) = 0$, where l is the thickness of the perovskite film.

The diffusion coefficient D can be obtained by fitting the observed TRPL curve with the above model. Then, the average diffusion length L_D is determined from $L_D = \sqrt{D\tau}$, where τ is the recombination lifetime in the absence of a quencher, and the mobility μ can be calculated according to the Einstein relation $\mu = \frac{q}{kT}D$.

Li *et al.* first, to the best of our knowledge, used the model to determine the diffusion length in all-inorganic $CsPbBr_3$ as well as the Cl-doped cubic $CsPbBr_3$(Cl) [50]. The obtained fitting result for orthorhombic $CsPbBr_3$ was around 69 nm, while the value of diffusion length for cubic $CsPbBr_3$ was 197 nm, and, for cubic $CsPbBr_3$(Cl), it was 208 nm. Cubic $CsPbBr_3$ and $CsPbBr_3$(Cl) revealed longer carrier lifetime and larger diffusion length than orthorhombic $CsPbBr_3$, even longer than the $CH_3NH_3PbI_3$ reported by Stranks *et al.* [132]. The superior photophysical properties of cubic $CsPbBr_3$ and $CsPbBr_3$(Cl) indicate that it can be a more suitable candidate for optoelectronic applications.

As for the $CsPbI_3$ perovskite material, the diffusion coefficient and diffusion length were extracted by fitting the TRPL spectra of three samples: neat $CsPbI_3$, $CsPbI_3$/PCBM, and $CsPbI_3$/Spiro-OMeTAD [87]. The diffusion coefficients for hole and electron of $CsPbI_3$ were calculated to be 0.0018 ± 0.0001 and 0.025 ± 0.001 $cm^2 \cdot s^{-1}$, respectively, and the corresponding diffusion lengths were up to 350 and 94 nm, which are comparable with the previously reported values for the polycrystalline $CH_3NH_3PbI_3$ thin films [132,133]. However, the unbalanced electron and hole transport properties in $CsPbI_3$ were still unrevealed and suspended for further investigation. Hu *et al.* employed a two-dimensional diffusion model to study the $CsPbI_3$ microcrystals [134]. After analyzing sixteen individual samples, the diffusion coefficient ranged from 0.6 to 1.2 $cm^2 \cdot s^{-1}$, and the diffusion length was estimated to be between 4 and 10 μm, which was much larger than the reported values.

Ning *et al.* studied the Pb-free halide double perovskite of $Cs_2AgBiBr_6$, $Cs_2AgBiBr_6$/$PC_{61}BM$, and $Cs_2AgBiBr_6$/Spiro–OMeTAD thoroughly [71]. The average carrier lifetime of pristine $Cs_2AgBiBr_6$ film was 13.7 ns by double exponential model fitting of the TRPL curve, while the obtained lifetimes for films with ETL (or HTL) were 2.4 ns (with $PC_{61}BM$) and 2.6 ns (with Spiro-OMeTAD), respectively. Further, by employing the above diffusion model, they calculated the average photoexcitation mobility of 0.37 $cm^2 \cdot V^{-1} \cdot s^{-1}$, and the diffusion length for electrons and holes of ~110 nm in $Cs_2AgBiBr_6$, which was comparable to those of Pb-based halide perovskite films possessing typical carrier diffusion length of 100 $nm^{-1} \cdot \mu m$ [94,95,132].

Chen *et al.* proposed a novel Pb-free cesium titanium bromide (Cs_2TiBr_6) perovskite thin film [135]. They chose TiO_2 and P_3HT as electron- and hole-quenching layers, respectively. Through single exponential fitting, the carrier lifetime was estimated to be 24 ns (pristine Cs_2TiBr_6), 2.5 ns (Cs_2TiBr_6/TiO_2), and 3.6 ns (Cs_2TiBr_6/P_3HT). Using the diffusion equation, the diffusion length was estimated at 121 nm for electrons and 103 nm for holes. The authors also mentioned that the quencher layers they employed may not be ideal for Cs_2TiBr_6, and thus the above diffusion length values were expected to be conservative. Nevertheless, the estimated diffusion length value approached those found in the popular $CH_3NH_3PbI_3$.

5. COMPARISON WITH SOME OTHER TECHNIQUES

A. Transient Absorption Spectroscopy

Although TRPL is a common method to investigate carrier dynamics and transport processes in halide perovskites, it still has certain disadvantages. For example, PL studies cannot resolve very fast decay components due to their limited instrument response function. Moreover, the observed PL signal only reflects the radiative recombination inside the material. Although the carrier participation in other dynamic processes will also influence the radiative recombination, those processes cannot be explored from the PL curve directly. In some situations, PLQY is used to characterize the proportion of carriers participating in radiative luminescence, since the value of PLQY can be considered as a result of competition between radiative and non-radiative processes [136]. It should be noted that some research groups have reported relatively lower PLQY values [28,137], which indicates that the dominant carrier dynamics in these materials is a non-radiative process. Therefore, other experimental techniques are required for supplement. At present, one of the most widely used techniques is transient absorption (TA) spectroscopy. Due to its ultrafast resolution time [in the order of femtosecond (fs)], it can be employed to detect more rapid non-radiative decay processes inside materials.

To gain a more comprehensive understanding of the carrier dynamic process, some research groups adopted TRPL and TA at the same time [28,29,138]. Zhou *et al.* analyzed the charge carrier dynamics of all-inorganic Pb-free Cs_2PdBr_6 perovskite NCs [29]. The average decay time is estimated to be 0.9 ns by fitting the TRPL curve with a three-exponential function. However, the measured PLQY for Cs_2PdBr_6 NCs is relatively low (0.3%), which might have resulted from the ultrafast charge trapping process. Therefore, TA spectroscopy characterizations were further carried out to provide supplementary analysis of the ultrafast carrier dynamics. As shown in Fig. 10(a), the TA dynamics were decomposed into three components, and each was assigned to a dynamic process. An ultrafast component (1.42 ps) was observed, and it was assigned to carrier trapping, probably attributed to the numerous surface defects on the NCs. The slow component (>3 ns) was attributed to the defect associated decay pathways [28]. As for the observed middle time component (34.8 ps), it was indexed to the electron–hole radiative recombination. However, this difference between TA and TRPL was not fully explained in their paper. All of the above-mentioned processes were given by a schematic diagram, as shown in Fig. 10(b).

Similar study was employed to analyze double perovskite $Cs_2AgBiBr_6$ NCs [28]. First, the PL decay was fitted by a three-exponential function, and the obtained short-lived (50 ps) and middle-lived (1 ns) components were assigned to the sub-band-gap transition and electron–hole radiative recombination, respectively. The long-lived component (100 ns) was assigned to the emission from sub-band-gap state [139]. The fs TA was employed to further investigate the non-radiative process due to the low PLQY of $Cs_2AgBiBr_6$ NCs. As shown in Fig. 10(c), the observed decay times of 0.2 and 0.8 ps were assigned to the relaxation of hot holes and electrons, respectively. Furthermore, the 1.4 ps (40 ps) decay component was related to hole (electron) trapping. The author argued that the

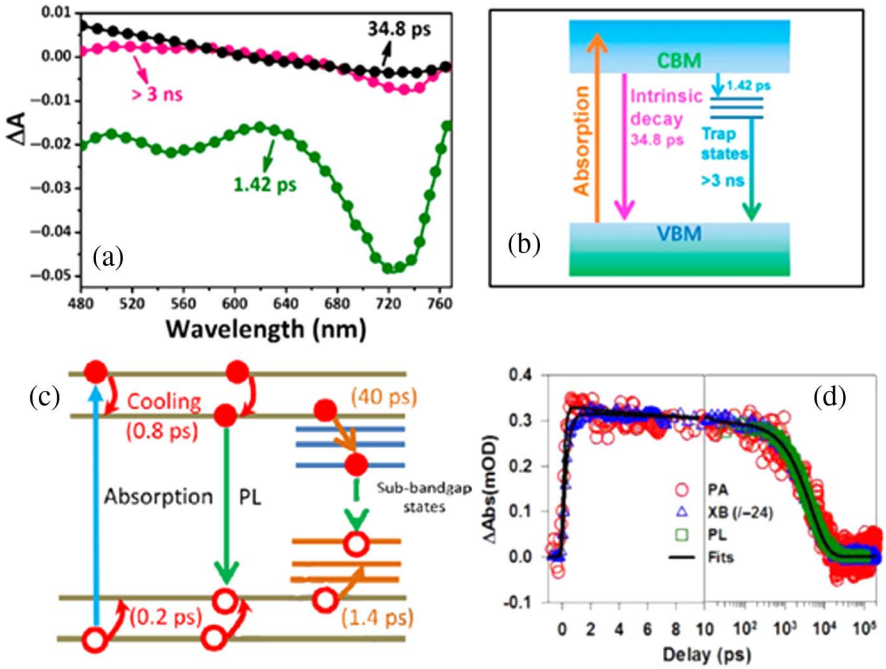

Fig. 10. (a) Decay associated spectra for three fitting components from TA spectra and (b) proposed excited dynamic model of Cs_2PdBr_6 NCs. Reprinted with permission [29]. (c) Charge carrier dynamic model of $Cs_2AgBiBr_6$ NCs. Reprinted with permission [28]. (d) Kinetics of XB (reduced by a factor of 24 and inverted), PA, and PL decay of $CsPbBr_3$ QDs. The black solid lines are multi-exponential fits to these kinetics. Reprinted with permission [140].

sub-band-gap TS may cause both radiative and non-radiative recombinations, which can be detected by both PL and TA.

It is interesting to note that exceptionally high PLQY (~79%) was observed in $CsPbBr_3$ perovskite QDs [140], and this phenomenon was then confirmed by ultrafast TA spectroscopy studies. Kinetics of transient features are shown in Fig. 10(d), where exciton bleach (XB), photo-induced absorption (PA), and PL decay curves agreed well with each other; although PL decay did not resolve fast decay components due to its limited instrument response function. The decay time constants (and amplitudes) of 8.4 ± 0.5 ps ($6.0\% \pm 0.5\%$) and 4.5 ± 0.2 ns ($94.0\% \pm 0.7\%$) were obtained by TA analysis. The relatively high percentage of the 4.5 ns decay process was assigned to the electron–hole radiative recombination, and it can also be detected by PL. Similarly, kinetic agreement between slow decay processes of TA and PL signals in $CsPbBr_3$ QDs was also observed by Li *et al.* [141].

B. Transient Photovoltage/Transient Photocurrent

The carrier lifetime of all-inorganic halide perovskite can also be investigated by other characterization techniques, including transient photovoltage (TPV), transient photocurrent (TPC) [49,51,124], time-resolved microwave conductivity (TRMC) [142], as well as intensity modulated photocurrent/photovoltage spectroscopy (IMPS/IMVS) [80]. The time calculated by the above measurements was found to be in the order of microseconds, much larger than those from TRPL and TA. We noticed that the reported studies were all employed in the PSCs, which means that the lifetime obtained may also be related to the external structure instead of the real dynamic process inside the perovskite film. Especially, for TPV, the difference between the extracted carrier lifetime and the intrinsic values was as high as 1 to 3 orders of magnitude, which has been quantitatively discussed by several researches [143–145] and will not be discussed here.

Nevertheless, the qualitative analyses by those measurements are still meaningful. For example, to study the effect of ZnO [51], MoO_3 [124], and $(CsPbI_2Br)_{1-x}(CsPbI_3)_x$ [49] intermediate layers in all-inorganic $CsPbI_2Br$ PSCs, respectively, the authors compared the carrier lifetimes calculated by TPV and TPC of $CsPbI_2Br$ PSCs with and without these target layers. As shown in Fig. 11, similar observations were

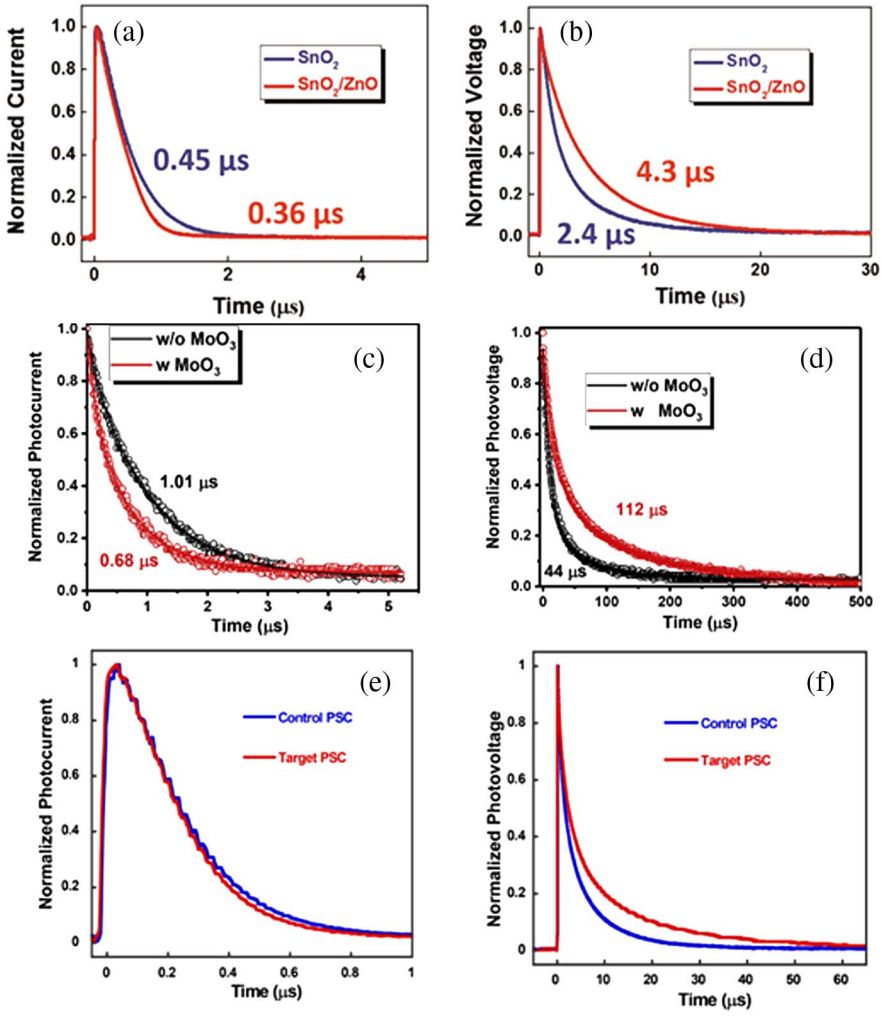

Fig. 11. (a) TPC and (b) TPV studies for SnO_2- and SnO_2/ZnO-based $CsPbI_2Br$ PSCs. Reprinted with permission [51]. (c) TPC and (d) TPV studies for $CsPbI_2Br$ film with or without MnO_3 layer. Reprinted with permission [124]. (e) TPC and (f) TPV studies for $CsPbI_2Br$ film with or without $(CsPbI_2Br)_{1-x}(CsPbI_3)_x$ layer. Reprinted with permission [49].

found in all three cases. The TPC decay lifetimes of the PSCs with target layers were shorter, while the charge recombination lifetimes from the TPV study of the PSCs with target layers were longer than those of the conventional PSCs. These phenomena can be explained because the charge recombination was slower and the extraction efficiency was enhanced by the reduction in charge traps with the existence of these target layers.

6. CONCLUSIONS AND PROSPECTS

We have reviewed the methods of exploring carrier dynamic processes by the PL technique and summarized the related results in recently reported all-inorganic halide perovskites. First, we discussed the bulk perovskite film, where the photo-generated carriers were mainly involved in recombination processes, i.e., radiative and non-radiative recombinations. Through fitting the power dependence of the SSPL integrated intensity and the excitation density, the mechanism of recombination can be estimated. More information about the carrier relaxation process can be deduced by utilizing the TRPL. Using the multiple exponential relation $I_{\mathrm{PL}}(t) = \sum_i A_i \exp(-\frac{t}{\tau_i}) + y_0$, the carrier lifetimes as well as their corresponding dynamic processes can be obtained, and the reported data simulated by the relation in all-inorganic halide perovskite materials were summarized in Table 1. It is found that for bulk thin film samples, two exponential terms were generally used, while for nanostructured materials, three exponential terms were needed, which indicates that the more complex the material structure, the more diversified the internal carrier recombination process. In addition, the excitation intensity dependency of PL intensity just after photoexcitation was also a way to study the nature of the radiative recombination.

Second, the PL properties of halide perovskite samples with TLs are investigated, where the dynamic process of photo-generated carriers is not only a recombination, but also a transfer to the TL. Compared with that of the pristine samples, the SSPL decreased sharply, and the TRPL curve became steeper due to the shorter carrier lifetime. To characterize the effect of TL on the transfer of photo-generated carriers in halide perovskite materials, the concept of transfer efficiency was introduced. We elaborated the relevant study reported in all-inorganic perovskite-based PSCs and sorted out the corresponding data in Table 3. In addition, the TRPL curve was also quantitatively fitted by a one-dimensional diffusion equation, through which other important transport characteristics, such as diffusion coefficient and length, can be simulated. It is found that the reported diffusion length in all-inorganic halide perovskite materials is in the range of 100 nm–10 μm, comparable or larger than those reported in hybrid perovskite samples.

Finally, we also briefly discussed other optoelectronic methods for studying carrier dynamics. Due to some limitations of instrument response, it is difficult to detect the very fast path by PL. Therefore, the combination of PL and TA is an effective choice to thoroughly investigate the photo-generated carrier dynamics. We also noticed that the carrier lifetime obtained by the TPV (TPC) test cannot accurately reflect the characteristics of carriers inside materials because of the influence from external structures. However, the qualitative conclusion is given for reference.

Overall, SSPL and TRPL are effective techniques to study the carrier dynamics of all-inorganic halide perovskites, and most researchers regard them as one of the necessary means for characterization. However, we note that most of the research groups only used the PL curve to obtain the corresponding carrier lifetime in all-inorganic halide perovskite materials [146–151]. There is neither further discussion on the external factors that will affect the carrier dynamics, such as growth method and doping, nor the internal physical explanation to the difference between the studied samples. Therefore, future investigation on these fields is still available and expected.

Funding. National Natural Science Foundation of China (61875119); Program for Professor of Special Appointment (Eastern Scholar) at Shanghai Institutions of Higher Learning; Shanghai Rising-Star Program (19QA1404000); Shanghai Education Development Foundation (18CG63).

Disclosures. The authors declare no conflicts of interest.

REFERENCES

1. M.-G. Ju, M. Chen, Y. Zhou, J. Dai, L. Ma, N. P. Padture, and X. C. Zeng, "Toward eco-friendly and stable perovskite materials for photovoltaics," Joule **2**, 1231–1241 (2018).
2. X. Zhou, J. Jankowska, H. Dong, and O. V. Prezhdo, "Recent theoretical progress in the development of perovskite photovoltaic materials," J. Energy Chem. **27**, 637–649 (2018).
3. J. Yang, B. D. Siempelkamp, D. Liu, and T. L. Kelly, "Investigation of $CH_3NH_3PbI_3$ degradation rates and mechanisms in controlled humidity environments using *in situ* techniques," ACS Nano **9**, 1955–1963 (2015).
4. T. A. Berhe, W.-N. Su, C.-H. Chen, C.-J. Pan, J.-H. Cheng, H.-M. Chen, M.-C. Tsai, L.-Y. Chen, A. A. Dubale, and B.-J. Hwang, "Organometal halide perovskite solar cells: degradation and stability," Energy Environ. Sci. **9**, 323–356 (2016).
5. Y. Yang and J. You, "Make perovskite solar cells stable," Nature **544**, 155–156 (2017).
6. Y. Han, S. Meyer, Y. Dkhissi, K. Weber, J. M. Pringle, U. Bach, L. Spiccia, and Y.-B. Cheng, "Degradation observations of encapsulated planar $CH_3NH_3PbI_3$ perovskite solar cells at high temperatures and humidity," J. Mater. Chem. A **3**, 8139–8147 (2015).
7. S. Chen, Y. Zhang, X. Zhang, J. Zhao, Z. Zhao, X. Su, Z. Hua, J. Zhang, J. Cao, and J. Feng, "General decomposition pathway of organic–inorganic hybrid perovskites through an intermediate superstructure and its suppression mechanism," Adv. Mater. **32**, 2001107 (2020).
8. Y. Jiang, J. Yuan, Y. Ni, J. Yang, Y. Wang, T. Jiu, M. Yuan, and J. Chen, "Reduced-dimensional α-$CsPbX_3$ perovskites for efficient and stable photovoltaics," Joule **2**, 1356–1368 (2018).
9. A. H. Slavney, T. Hu, A. M. Lindenberg, and H. I. Karunadasa, "A bismuth-halide double perovskite with long carrier recombination lifetime for photovoltaic applications," J. Am. Chem. Soc. **138**, 2138–2141 (2016).
10. J. Duan, Y. Zhao, B. He, and Q. Tang, "High-purity inorganic perovskite films for solar cells with 9.72% efficiency," Angew. Chem. (Int. Ed.) **57**, 3787–3791 (2018).
11. F. Locardi, M. Cirignano, D. Baranov, Z. Dang, M. Prato, F. Drago, M. Ferretti, V. Pinchetti, M. Fanciulli, and S. Brovelli, "Colloidal synthesis of double perovskite $Cs_2AgInCl_6$ and Mn-doped $Cs_2AgInCl_6$ nanocrystals," J. Am. Chem. Soc. **140**, 12989–12995 (2018).
12. D. Shi, V. Adinolfi, R. Comin, M. Yuan, E. Alarousu, A. Buin, Y. Chen, S. Hoogland, A. Rothenberger, and K. Katsiev, "Low trap-state

density and long carrier diffusion in organolead trihalide perovskite single crystals," Science **347**, 519–522 (2015).
13. C. Wehrenfennig, G. E. Eperon, M. B. Johnston, H. J. Snaith, and L. M. Herz, "High charge carrier mobilities and lifetimes in organolead trihalide perovskites," Adv. Mater. **26**, 1584–1589 (2014).
14. S. De Wolf, J. Holovsky, S.-J. Moon, P. Löper, B. Niesen, M. Ledinsky, F.-J. Haug, J.-H. Yum, and C. Ballif, "Organometallic halide perovskites: sharp optical absorption edge and its relation to photovoltaic performance," J. Phys. Chem. Lett. **5**, 1035–1039 (2014).
15. X. Li, F. Cao, D. Yu, J. Chen, Z. Sun, Y. Shen, Y. Zhu, L. Wang, Y. Wei, and Y. Wu, "All inorganic halide perovskites nanosystem: synthesis, structural features, optical properties and optoelectronic applications," Small **13**, 1603996 (2017).
16. Y. Wang, X. Li, J. Song, L. Xiao, H. Zeng, and H. Sun, "All-inorganic colloidal perovskite quantum dots: a new class of lasing materials with favorable characteristics," Adv. Mater. **27**, 7101–7108 (2015).
17. J. Kwak, W. K. Bae, D. Lee, I. Park, J. Lim, M. Park, H. Cho, H. Woo, D. Y. Yoon, and K. Char, "Bright and efficient full-color colloidal quantum dot light-emitting diodes using an inverted device structure," Nano Lett. **12**, 2362–2366 (2012).
18. G. Nedelcu, L. Protesescu, S. Yakunin, M. I. Bodnarchuk, M. J. Grotevent, and M. V. Kovalenko, "Fast anion-exchange in highly luminescent nanocrystals of cesium lead halide perovskites ($CsPbX_3$, X= Cl, Br, I)," Nano Lett. **15**, 5635–5640 (2015).
19. Q. Shan, J. Song, Y. Zou, J. Li, L. Xu, J. Xue, Y. Dong, B. Han, J. Chen, and H. Zeng, "High performance metal halide perovskite light-emitting diode: from material design to device optimization," Small **13**, 1701770 (2017).
20. Z. Shi, Y. Li, Y. Zhang, Y. Chen, X. Li, D. Wu, T. Xu, C. Shan, and G. Du, "High-efficiency and air-stable perovskite quantum dots light-emitting diodes with an all-inorganic heterostructure," Nano Lett. **17**, 313–321 (2017).
21. S. Yakunin, L. Protesescu, F. Krieg, M. I. Bodnarchuk, G. Nedelcu, M. Humer, G. De Luca, M. Fiebig, W. Heiss, and M. V. Kovalenko, "Low-threshold amplified spontaneous emission and lasing from colloidal nanocrystals of caesium lead halide perovskites," Nat. Commun. **6**, 8056 (2015).
22. L. N. Quan, F. P. García de Arquer, R. P. Sabatini, and E. H. Sargent, "Perovskites for light emission," Adv. Mater. **30**, 1801996 (2018).
23. Z. Shi, S. Li, Y. Li, H. Ji, X. Li, D. Wu, T. Xu, Y. Chen, Y. Tian, and Y. Zhang, "Strategy of solution-processed all-inorganic heterostructure for humidity/temperature-stable perovskite quantum dot light-emitting diodes," ACS Nano **12**, 1462–1472 (2018).
24. J. Lin, M. Lai, L. Dou, C. S. Kley, H. Chen, F. Peng, J. Sun, D. Lu, S. A. Hawks, C. Xie, F. Cui, A. P. Alivisatos, D. T. Limmer, and P. Yang, "Thermochromic halide perovskite solar cells," Nat. Mater. **17**, 261–267 (2018).
25. T. J. S. Evans, A. Schlaus, Y. Fu, X. Zhong, T. L. Atallah, M. S. Spencer, L. E. Brus, S. Jin, and X. Y. Zhu, "Continuous-wave lasing in cesium lead bromide perovskite nanowires," Adv. Opt. Mater. **6**, 1700982 (2018).
26. N. Wang, L. Cheng, R. Ge, S. Zhang, Y. Miao, W. Zou, C. Yi, Y. Sun, Y. Cao, and R. Yang, "Perovskite light-emitting diodes based on solution-processed self-organized multiple quantum wells," Nat. Photonics **10**, 699–704 (2016).
27. H. Shi, X. Zhang, X. Sun, R. Chen, and X. Zhang, "Direct and indirect recombination and thermal kinetics of excitons in colloidal all-inorganic lead halide perovskite nanocrystals," J. Phys. Chem. C **123**, 19844–19850 (2019).
28. B. Yang, J. Chen, S. Yang, F. Hong, L. Sun, P. Han, T. Pullerits, W. Deng, and K. Han, "Lead-free silver-bismuth halide double perovskite nanocrystals," Angew. Chem. (Int. Ed.) **130**, 5457–5461 (2018).
29. L. Zhou, J.-F. Liao, Z.-G. Huang, X.-D. Wang, Y.-F. Xu, H.-Y. Chen, D.-B. Kuang, and C.-Y. Su, "All-inorganic lead-free Cs_2PdX_6 (X= Br, I) perovskite nanocrystals with single unit cell thickness and high stability," ACS Energy Lett. **3**, 2613–2619 (2018).
30. V. D'Innocenzo, A. R. Srimath Kandada, M. De Bastiani, M. Gandini, and A. Petrozza, "Tuning the light emission properties by band gap engineering in hybrid lead halide perovskite," J. Am. Chem. Soc. **136**, 17730–17733 (2014).
31. B. Dänekamp, N. Droseros, F. Palazon, M. Sessolo, N. Banerji, and H. J. Bolink, "Efficient photo- and electroluminescence by trap states passivation in vacuum-deposited hybrid perovskite thin films," ACS Appl. Mater. Interfaces **10**, 36187–36193 (2018).
32. S. B. Naghadeh, B. Luo, Y.-C. Pu, Z. Schwartz, W. R. Hollingsworth, S. A. Lindley, A. S. Brewer, A. L. Ayzner, and J. Z. Zhang, "Size dependence of charge carrier dynamics in organometal halide perovskite nanocrystals: deciphering radiative versus nonradiative components," J. Phys. Chem. C **123**, 4610–4619 (2019).
33. B. A. Koscher, J. K. Swabeck, N. D. Bronstein, and A. P. Alivisatos, "Essentially trap-free $CsPbBr_3$ colloidal nanocrystals by postsynthetic thiocyanate surface treatment," J. Am. Chem. Soc. **139**, 6566–6569 (2017).
34. V. S. Chirvony, S. González-Carrero, I. Suárez, R. E. Galian, M. Sessolo, H. J. Bolink, J. P. Martínez-Pastor, and J. Pérez-Prieto, "Delayed luminescence in lead halide perovskite nanocrystals," J. Phys. Chem. C **121**, 13381–13390 (2017).
35. M. A. Becker, L. Scarpelli, G. Nedelcu, G. Rainò, F. Masia, P. Borri, T. Stöferle, M. V. Kovalenko, W. Langbein, and R. F. Mahrt, "Long exciton dephasing time and coherent phonon coupling in $CsPbBr_2Cl$ perovskite nanocrystals," Nano Lett. **18**, 7546–7551 (2018).
36. J.-S. Yao, J. Ge, B.-N. Han, K.-H. Wang, H.-B. Yao, H.-L. Yu, J.-H. Li, B.-S. Zhu, J.-Z. Song, and C. Chen, "Ce^{3+}-doping to modulate photoluminescence kinetics for efficient $CsPbBr_3$ nanocrystals based light-emitting diodes," J. Am. Chem. Soc. **140**, 3626–3634 (2018).
37. Y. Yamada, T. Yamada, A. Shimazaki, A. Wakamiya, and Y. Kanemitsu, "Interfacial charge-carrier trapping in $CH_3NH_3PbI_3$-based heterolayered structures revealed by time-resolved photoluminescence spectroscopy," J. Phys. Chem. Lett. **7**, 1972–1977 (2016).
38. A. Marchioro, P. J. Whitham, H. D. Nelson, M. C. De Siena, K. E. Knowles, V. Z. Polinger, P. J. Reid, and D. R. Gamelin, "Strong dependence of quantum-dot delayed luminescence on excitation pulse width," J. Phys. Chem. Lett. **8**, 3997–4003 (2017).
39. X. Yuan, S. Ji, M. C. De Siena, L. Fei, Z. Zhao, Y. Wang, H. Li, J. Zhao, and D. R. Gamelin, "Photoluminescence temperature dependence, dynamics, and quantum efficiencies in Mn^{2+}-doped $CsPbCl_3$ perovskite nanocrystals with varied dopant concentration," Chem. Mater. **29**, 8003–8011 (2017).
40. P. Strak, K. Koronski, K. Sakowski, K. Sobczak, J. Borysiuk, K. P. Korona, P. A. Drozdz, E. Grzanka, M. Sarzynski, A. Suchocki, E. Monroy, S. Krukowski, and A. Kaminska, "Instantaneous decay rate analysis of time resolved photoluminescence (TRPL): application to nitrides and nitride structures," J. Alloys Compd. **823**, 153791 (2020).
41. C. M. Sutter-Fella, Y. Li, M. Amani, J. W. Ager III, F. M. Toma, E. Yablonovitch, I. D. Sharp, and A. Javey, "High photoluminescence quantum yield in band gap tunable bromide containing mixed halide perovskites," Nano Lett. **16**, 800–806 (2016).
42. M. S. Hajime Shibata, A. Yamada, K. Matsubara, K. Sakurai, H. Tampo, S. Ishizuka, K.-K. Kim, and S. Niki, "Excitation-power dependence of free exciton photoluminescence of semiconductors," Jpn. J. Appl. Phys. **44**, 6113–6114 (2005).
43. M. Saba, M. Cadelano, D. Marongiu, F. Chen, V. Sarritzu, N. Sestu, C. Figus, M. Aresti, R. Piras, and A. G. Lehmann, "Correlated electron–hole plasma in organometal perovskites," Nat. Commun. **5**, 5049 (2014).
44. Y. Wang, M. Zhi, Y.-Q. Chang, J.-P. Zhang, and Y. Chan, "Stable, ultralow threshold amplified spontaneous emission from $CsPbBr_3$ nanoparticles exhibiting trion gain," Nano Lett. **18**, 4976–4984 (2018).
45. D. Bimberg, M. Sondergeld, and E. Grobe, "Thermal dissociation of excitons bounds to neutral acceptors in high-purity GaAs," Phys. Rev. B **4**, 3451–3455 (1971).
46. L. Jiang, Z. Fang, H. Lou, C. Lin, Z. Chen, J. Li, H. He, and Z. Ye, "Achieving long carrier lifetime and high optical gain in all-inorganic $CsPbBr_3$ perovskite films via top and bottom surface modification," Phys. Chem. Chem. Phys. **21**, 21996–22001 (2019).
47. Z. Liu, Q. Shang, C. Li, L. Zhao, Y. Gao, Q. Li, J. Chen, S. Zhang, X. Liu, Y. Fu, and Q. Zhang, "Temperature-dependent photoluminescence and lasing properties of $CsPbBr_3$ nanowires," Appl. Phys. Lett. **114**, 101902 (2019).

48. Q. Shang, M. Li, L. Zhao, D. Chen, S. Zhang, S. Chen, P. Gao, C. Shen, J. Xing, G. Xing, B. Shen, X. Liu, and Q. Zhang, "Role of the exciton-polariton in a continuous-wave optically pumped $CsPbBr_3$ perovskite laser," Nano Lett. **20**, 6636–6643 (2020).
49. W. Xu, F. He, M. Zhang, P. Nie, S. Zhang, C. Zhao, R. Luo, J. Li, X. Zhang, and S. Zhao, "Minimizing voltage loss in efficient all-inorganic $CsPbI_2Br$ perovskite solar cells through energy level alignment," ACS Energy Lett. **4**, 2491–2499 (2019).
50. B. Li, Y. Zhang, L. Zhang, and L. Yin, "$PbCl_2$-tuned inorganic cubic $CsPbBr_3$(Cl) perovskite solar cells with enhanced electron lifetime, diffusion length and photovoltaic performance," J. Power Sources **360**, 11–20 (2017).
51. L. Yan, Q. Xue, M. Liu, Z. Zhu, J. Tian, Z. Li, Z. Chen, Z. Chen, H. Yan, and H. L. Yip, "Interface engineering for all-inorganic $CsPbI_2Br$ perovskite solar cells with efficiency over 14%," Adv. Mater. **30**, 1802509 (2018).
52. D. Ghosh, M. Y. Ali, D. K. Chaudhary, and S. Bhattacharyya, "Dependence of halide composition on the stability of highly efficient all-inorganic cesium lead halide perovskite quantum dot solar cells," Sol. Energy Mater. Sol. Cells **185**, 28–35 (2018).
53. Y. Ren, Y. Hao, N. Zhang, Z. Arain, M. Mateen, Y. Sun, P. Shi, M. Cai, and S. Dai, "Exploration of polymer-assisted crystallization kinetics in $CsPbBr_3$ all-inorganic solar cell," Chem. Eng. J. **392**, 123805 (2020).
54. M. Wu, K. Yan, Y. Wang, and X. Kang, "High crystallinity and photovoltaic performance of $CsPbI_3$ film enabled by secondary dimension," J. Energy Chem. **48**, 181–186 (2020).
55. W. Chen, H. Chen, G. Xu, R. Xue, S. Wang, Y. Li, and Y. Li, "Precise control of crystal growth for highly efficient $CsPbI_2Br$ perovskite solar cells," Joule **3**, 191–204 (2019).
56. D. H. Kim, J. H. Heo, and S. H. Im, "Hysteresis-less $CsPbI_2Br$ mesoscopic perovskite solar cells with a high open-circuit voltage exceeding 1.3 V and 14.86% of power conversion efficiency," ACS Appl. Mater. Interfaces **11**, 19123–19131 (2019).
57. J. K. Nam, S. U. Chai, W. Cha, Y. J. Choi, W. Kim, M. S. Jung, J. Kwon, D. Kim, and J. H. Park, "Potassium incorporation for enhanced performance and stability of fully inorganic cesium lead halide perovskite solar cells," Nano Lett. **17**, 2028–2033 (2017).
58. C. F. J. Lau, M. Zhang, X. Deng, J. Zheng, J. Bing, Q. Ma, J. Kim, L. Hu, M. A. Green, and S. Huang, "Strontium-doped low-temperature-processed $CsPbI_2Br$ perovskite solar cells," ACS Energy Lett. **2**, 2319–2325 (2017).
59. C. F. J. Lau, X. Deng, J. Zheng, J. Kim, Z. Zhang, M. Zhang, J. Bing, B. Wilkinson, L. Hu, R. Patterson, S. Huang, and A. Ho-Baillie, "Enhanced performance via partial lead replacement with calcium for a $CsPbI_3$ perovskite solar cell exceeding 13% power conversion efficiency," J. Mater. Chem. A **6**, 5580–5586 (2018).
60. Z. Guo, S. Zhao, A. Liu, Y. Kamata, S. Teo, S. Yang, Z. Xu, S. Hayase, and T. Ma, "Niobium incorporation into $CsPbI_2Br$ for stable and efficient all-inorganic perovskite solar cells," ACS Appl. Mater. Interfaces **11**, 19994–20003 (2019).
61. S. S. Mali, J. V. Patil, and C. K. Hong, "Hot-air-assisted fully air-processed barium incorporated $CsPbI_2Br$ perovskite thin films for highly efficient and stable all-inorganic perovskite solar cells," Nano Lett. **19**, 6213–6220 (2019).
62. S. Chen, T. Zhang, X. Liu, J. Qiao, L. Peng, J. Wang, Y. Liu, T. Yang, and J. Lin, "Lattice reconstruction of La-incorporated $CsPbI_2Br$ with suppressed phase transition for air-processed all-inorganic perovskite solar cells," J. Mater. Chem. C **8**, 3351–3358 (2020).
63. X. Liu, X. Tan, Z. Liu, H. Ye, B. Sun, T. Shi, Z. Tang, and G. Liao, "Boosting the efficiency of carbon-based planar $CsPbBr_3$ perovskite solar cells by a modified multistep spin-coating technique and interface engineering," Nano Energy **56**, 184–195 (2019).
64. A. Surendran, X. Yu, R. Begum, Y. Tao, Q. J. Wang, and W. L. Leong, "All inorganic mixed halide perovskite nanocrystal-graphene hybrid photodetector: from ultrahigh gain to photostability," ACS Appl. Mater. Interfaces **11**, 27064–27072 (2019).
65. X. Wan, Z. Yu, W. Tian, F. Huang, S. Jin, X. Yang, Y.-B. Cheng, A. Hagfeldt, and L. Sun, "Efficient and stable planar all-inorganic perovskite solar cells based on high-quality $CsPbBr_3$ films with controllable morphology," J. Energy Chem. **46**, 8–15 (2020).
66. Q. Zeng, X. Zhang, X. Feng, S. Lu, Z. Chen, X. Yong, S. A. Redfern, H. Wei, H. Wang, and H. Shen, "Polymer-passivated inorganic cesium lead mixed-halide perovskites for stable and efficient solar cells with high open-circuit voltage over 1.3 V," Adv. Mater. **30**, 1705393 (2018).
67. H. Chen, A. Guo, X. Gu, and M. Feng, "Highly luminescent $CsPbX_3$ (X= Cl, Br, I) perovskite nanocrystals with tunable photoluminescence properties," J. Alloys Compd. **789**, 392–399 (2019).
68. Y.-K. Ren, X.-Q. Shi, X.-H. Ding, J. Zhu, T. Hayat, A. Alsaedi, Z.-Q. Li, X.-X. Xu, S.-F. Yang, and S.-Y. Dai, "Facile fabrication of perovskite layers with large grains through a solvent exchange approach," Inorg. Chem. Front. **5**, 348–353 (2018).
69. Y.-K. Ren, X.-H. Ding, Y.-H. Wu, J. Zhu, T. Hayat, A. Alsaedi, Y.-F. Xu, Z.-Q. Li, S.-F. Yang, and S.-Y. Dai, "Temperature-assisted rapid nucleation: a facile method to optimize the film morphology for perovskite solar cells," J. Mater. Chem. A **5**, 20327–20333 (2017).
70. L. Zhang, X. Yang, Q. Jiang, P. Wang, Z. Yin, X. Zhang, H. Tan, Y. M. Yang, M. Wei, and B. R. Sutherland, "Ultra-bright and highly efficient inorganic based perovskite light-emitting diodes," Nat. Commun. **8**, 15640 (2017).
71. W. Ning, F. Wang, B. Wu, J. Lu, Z. Yan, X. Liu, Y. Tao, J. M. Liu, W. Huang, and M. Fahlman, "Long electron–hole diffusion length in high-quality lead-free double perovskite films," Adv. Mater. **30**, 1706246 (2018).
72. Z. Yang, X. Zhang, W. Yang, G. E. Eperon, and D. S. Ginger, "Tin–lead alloying for efficient and stable all-inorganic perovskite solar cells," Chem. Mater. **32**, 2782–2794 (2020).
73. C. Wang, J. Zhang, J. Duan, L. Gong, J. Wu, L. Jiang, C. Zhou, H. Xie, Y. Gao, and H. He, "All-inorganic, hole-transporting-layer-free, carbon-based $CsPbIBr_2$ planar perovskite solar cells by a two-step temperature-control annealing process," Mater. Sci. Semicond. Process. **108**, 104870 (2020).
74. Y. Yuan, M. Chen, S. Yang, X. Shen, Y. Liu, and D. Cao, "Exciton recombination mechanisms in solution grown single crystalline $CsPbBr_3$ perovskite," J. Lumin. **226**, 117471 (2020).
75. J. Deng, J. Xun, and R. He, "Facile and rapid synthesis of high performance perovskite nanocrystals $CsPb(X/Br)_3$ (X= Cl, I) at room temperature," Opt. Mater. **99**, 109528 (2020).
76. D. Lu, Y. Zhang, M. Lai, A. Lee, C. Xie, J. Lin, T. Lei, Z. Lin, C. S. Kley, J. Huang, E. Rabani, and P. Yang, "Giant light-emission enhancement in lead halide perovskites by surface oxygen passivation," Nano Lett. **18**, 6967–6973 (2018).
77. J. Lin, H. Chen, J. Kang, L. N. Quan, Z. Lin, Q. Kong, M. Lai, S. Yu, L. Wang, and L.-W. Wang, "Copper (I)-based highly emissive all-inorganic rare-earth halide clusters," Matter **1**, 180–191 (2019).
78. W. Zhao, Z. Yao, F. Yu, D. Yang, and S. Liu, "Alkali metal doping for improved $CH_3NH_3PbI_3$ perovskite solar cells," Adv. Sci. **5**, 1700131 (2018).
79. W. Zhao, D. Yang, Z. Yang, and S. F. Liu, "Zn-doping for reduced hysteresis and improved performance of methylammonium lead iodide perovskite hybrid solar cells," Mater. Today Energy **5**, 205–213 (2017).
80. S. Xiang, W. Li, Y. Wei, J. Liu, H. Liu, L. Zhu, and H. Chen, "The synergistic effect of non-stoichiometry and Sb-doping on air-stable α-$CsPbI_3$ for efficient carbon-based perovskite solar cells," Nanoscale **10**, 9996–10004 (2018).
81. Q. Dong, Z. Wang, K. Zhang, H. Yu, P. Huang, X. Liu, Y. Zhou, N. Chen, and B. Song, "Easily accessible polymer additives for tuning the crystal-growth of perovskite thin-films for highly efficient solar cells," Nanoscale **8**, 5552–5558 (2016).
82. M. Hadadian, J. P. Correa-Baena, E. K. Goharshadi, A. Ummadisingu, J. Y. Seo, J. Luo, S. Gholipour, S. M. Zakeeruddin, M. Saliba, and A. Abate, "Enhancing efficiency of perovskite solar cells via N-doped graphene: crystal modification and surface passivation," Adv. Mater. **28**, 8681–8686 (2016).
83. K. Thesika and A. V. Murugan, "Microwave-enhanced chemistry at solid-liquid interfaces: synthesis of all-inorganic $CsPbX_3$ nanocrystals and unveiling the anion-induced evolution of structural and optical properties," Inorg. Chem. **59**, 6161–6175 (2020).

84. X. Chen, H. Lu, Y. Yang, and M. C. Beard, "Excitonic effects in methylammonium lead halide perovskites," J. Phys. Chem. Lett. **9**, 2595–2603 (2018).
85. H. He, Q. Yu, H. Li, J. Li, J. Si, Y. Jin, N. Wang, J. Wang, J. He, X. Wang, Y. Zhang, and Z. Ye, "Exciton localization in solution-processed organolead trihalide perovskites," Nat. Commun. **7**, 10896 (2016).
86. Q. Shang, S. Zhang, Z. Liu, J. Chen, P. Yang, C. Li, W. Li, Y. Zhang, Q. Xiong, X. Liu, and Q. Zhang, "Surface plasmon enhanced strong exciton-photon coupling in hybrid inorganic-organic perovskite nanowires," Nano Lett. **18**, 3335–3343 (2018).
87. Y. Fu, M. T. Rea, J. Chen, D. J. Morrow, M. P. Hautzinger, Y. Zhao, D. Pan, L. H. Manger, J. C. Wright, and R. H. Goldsmith, "Selective stabilization and photophysical properties of metastable perovskite polymorphs of $CsPbI_3$ in thin films," Chem. Mater. **29**, 8385–8394 (2017).
88. Y. Zhu, G. Pan, L. Shao, G. Yang, X. Xu, J. Zhao, and Y. Mao, "Effective infrared emission of erbium ions doped inorganic lead halide perovskite quantum dots by sensitization of ytterbium ions," J. Alloys Compd. **835**, 155390 (2020).
89. X. Zhang, Y. Zhang, X. Zhang, W. Yin, Y. Wang, H. Wang, M. Lu, Z. Li, Z. Gu, and W. Y. William, "Yb^{3+} and Yb^{3+}/Er^{3+} doping for near-infrared emission and improved stability of $CsPbCl_3$ nanocrystals," J. Mater. Chem. C **6**, 10101–10105 (2018).
90. G. Pan, X. Bai, W. Xu, X. Chen, D. Zhou, J. Zhu, H. Shao, Y. Zhai, B. Dong, and L. Xu, "Impurity ions codoped cesium lead halide perovskite nanocrystals with bright white light emission toward ultraviolet–white light-emitting diode," ACS Appl. Mater. Interfaces **10**, 39040–39048 (2018).
91. A. Dey, P. Rathod, and D. Kabra, "Role of localized states in photoluminescence dynamics of high optical gain $CsPbBr_3$ nanocrystals," Adv. Opt. Mater. **6**, 1800109 (2018).
92. T. Schmidt, G. Daniel, and K. Lischka, "The excitation power dependence of the near band edge photoluminescence of II-VI semiconductors," J. Cryst. Growth **117**, 748–752 (1992).
93. B. Wu, Y. Zhou, G. Xing, Q. Xu, H. F. Garces, A. Solanki, T. W. Goh, N. P. Padture, and T. C. Sum, "Long minority-carrier diffusion length and low surface-recombination velocity in inorganic lead-free $CsSnI_3$ perovskite crystal for solar cells," Adv. Funct. Mater. **27**, 1604818 (2017).
94. Y. Yamada, T. Nakamura, M. Endo, A. Wakamiya, and Y. Kanemitsu, "Photocarrier recombination dynamics in perovskite $CH_3NH_3PbI_3$ for solar cell applications," J. Am. Chem. Soc. **136**, 11610–11613 (2014).
95. G. Xing, N. Mathews, S. Sun, S. S. Lim, Y. M. Lam, M. Grätzel, S. Mhaisalkar, and T. C. Sum, "Long-range balanced electron- and hole-transport lengths in organic-inorganic $CH_3NH_3PbI_3$," Science **342**, 344–347 (2013).
96. C. Li, L. Zhao, H. Fan, Q. Shang, W. Du, J. Shi, Y. Zhao, X. Liu, and Q. Zhang, "Graphoepitaxy of large scale, highly ordered $CsPbBr_3$ nanowire array on muscovite mica (001) driven by surface reconstructed grooves," Adv. Opt. Mater. **8**, 2000743 (2020).
97. Z. Wu, J. Chen, Y. Mi, X. Sui, S. Zhang, W. Du, R. Wang, J. Shi, X. Wu, X. Qiu, Z. Qin, Q. Zhang, and X. Liu, "All-inorganic $CsPbBr_3$ nanowire based plasmonic lasers," Adv. Opt. Mater. **6**, 1800674 (2018).
98. Y. Mi, Z. Liu, Q. Shang, X. Niu, J. Shi, S. Zhang, J. Chen, W. Du, Z. Wu, R. Wang, X. Qiu, X. Hu, Q. Zhang, T. Wu, and X. Liu, "Fabry–Perot oscillation and room temperature lasing in perovskite cube-corner pyramid cavities," Small **14**, 1703136 (2018).
99. P. Jing, J. Zheng, M. Ikezawa, X. Liu, S. Lv, X. Kong, J. Zhao, and Y. Masumoto, "Temperature-dependent photoluminescence of CdSe-core CdS/CdZnS/ZnS-multishell quantum dots," J. Phys. Chem. C **113**, 13545–13550 (2009).
100. W. Du, S. Zhang, Z. Wu, Q. Shang, Y. Mi, J. Chen, C. Qin, X. Qiu, Q. Zhang, and X. Liu, "Unveiling lasing mechanism in $CsPbBr_3$ microsphere cavities," Nanoscale **11**, 3145–3153 (2019).
101. K. Wu, A. Bera, C. Ma, Y. Du, Y. Yang, L. Li, and T. Wu, "Temperature-dependent excitonic photoluminescence of hybrid organometal halide perovskite films," Phys. Chem. Chem. Phys. **16**, 22476–22481 (2014).
102. J. Dai, H. Zheng, C. Zhu, J. Lu, and C. Xu, "Comparative investigation on temperature-dependent photoluminescence of $CH_3NH_3PbBr_3$ and $CH(NH_2)_2PbBr_3$ microstructures," J. Mater. Chem. C **4**, 4408–4413 (2016).
103. S. M. Lee, C. J. Moon, H. Lim, Y. Lee, M. Y. Choi, and J. Bang, "Temperature-dependent photoluminescence of cesium lead halide perovskite quantum dots: splitting of the photoluminescence peaks of $CsPbBr_3$ and $CsPb(Br/I)_3$ quantum dots at low temperature," J. Phys. Chem. C **121**, 26054–26062 (2017).
104. J. Li, X. Yuan, P. Jing, J. Li, M. Wei, J. Hua, J. Zhao, and L. Tian, "Temperature-dependent photoluminescence of inorganic perovskite nanocrystal films," RSC Adv. **6**, 78311–78316 (2016).
105. B. T. Diroll, H. Zhou, and R. D. Schaller, "Low-temperature absorption, photoluminescence, and lifetime of $CsPbX_3$ (X = Cl, Br, I) nanocrystals," Adv. Funct. Mater. **28**, 1800945 (2018).
106. A. Shinde, R. Gahlaut, and S. Mahamuni, "Low-temperature photoluminescence studies of $CsPbBr_3$ quantum dots," J. Phys. Chem. C **121**, 14872–14878 (2017).
107. K. Wei, Z. Xu, R. Chen, X. Zheng, X. Cheng, and T. Jiang, "Temperature-dependent excitonic photoluminescence excited by two-photon absorption in perovskite $CsPbBr_3$ quantum dots," Opt. Lett. **41**, 3821–3824 (2016).
108. Q. Han, W. Wu, W. Liu, Q. Yang, and Y. Yang, "Temperature-dependent photoluminescence of $CsPbX_3$ nanocrystal films," J. Lumin. **198**, 350–356 (2018).
109. X. Yuan, X. Hou, J. Li, C. Qu, W. Zhang, J. Zhao, and H. Li, "Thermal degradation of luminescence in inorganic perovskite $CsPbBr_3$ nanocrystals," Phys. Chem. Chem. Phys. **19**, 8934–8940 (2017).
110. Y. Gao, L. Zhao, Q. Y. Shang, C. Li, Z. Liu, Q. Li, X. N. Wang, and Q. Zhang, "Photoluminescence properties of ultrathin $CsPbCl_3$ nanowires on mica substrate," J. Semicond. **40**, 052201 (2019).
111. Y. Gao, L. Zhao, Q. Shang, Y. Zhong, Z. Liu, J. Chen, Z. Zhang, J. Shi, W. Du, Y. Zhang, S. Chen, P. Gao, X. Liu, X. Wang, and Q. Zhang, "Ultrathin $CsPbX_3$ nanowire arrays with strong emission anisotropy," Adv. Mater. **30**, 1801805 (2018).
112. T. T. K. Tanaka, T. Ban, T. Kondo, K. Uchida, and N. Miura, "Comparative study on the excitons in lead-halide-based perovskite-type crystals $CH_3NH_3PbBr_3$ $CH_3NH_3PbI_3$," Solid State Commun. **127**, 619–623 (2003).
113. M. Baranowski, P. Plochocka, R. Su, L. Legrand, T. Barisien, F. Bernardot, Q. Xiong, C. Testelin, and M. Chamarro, "Exciton binding energy and effective mass of $CsPbCl_3$: a magneto-optical study," Photon. Res. **8**, A50–A55 (2020).
114. Y. Zhao, C. Riemersma, F. Pietra, R. Koole, C. D. M. Donega, and A. Meijerink, "High-temperature luminescence quenching of colloidal quantum dots," ACS Nano **6**, 9058–9067 (2012).
115. C.-X. Qian, Z.-Y. Deng, K. Yang, J. Feng, M.-Z. Wang, Z. Yang, S. Liu, and H.-J. Feng, "Interface engineering of $CsPbBr_3/TiO_2$ heterostructure with enhanced optoelectronic properties for all-inorganic perovskite solar cells," Appl. Phys. Lett. **112**, 093901 (2018).
116. C. Chen, C. Wu, X. Ding, Y. Tian, M. Zheng, M. Cheng, H. Xu, Z. Jin, and L. Ding, "Constructing binary electron transport layer with cascade energy level alignment for efficient $CsPbI_2Br$ solar cells," Nano Energy **71**, 104604 (2020).
117. S. Yang, H. Zhao, M. Wu, S. Yuan, Y. Han, Z. Liu, K. Guo, S. F. Liu, S. Yang, and H. Zhao, "Highly efficient and stable planar $CsPbI_2Br$ perovskite solar cell with a new sensitive-dopant-free hole transport layer obtained via an effective surface passivation," Sol. Energy Mater. Sol. Cells **201**, 110052 (2019).
118. S. Yang, L. Wang, L. Gao, J. Cao, Q. Han, F. Yu, Y. Kamata, C. Zhang, M. Fan, and G. Wei, "Excellent moisture stability and efficiency of inverted all-inorganic $CsPbIBr_2$ perovskite solar cells through molecule interface engineering," ACS Appl. Mater. Interfaces **12**, 13931–13940 (2020).
119. Y. Liu, X. Zhao, Z. Yang, Q. Li, W. Wei, B. Hu, and W. Chen, "$Cu_{12}Sb_4S_{13}$ quantum dots with ligand exchange as hole transport materials in all-inorganic perovskite $CsPbI_3$ quantum dot solar cells," ACS Appl. Energy Mater. **3**, 3521–3529 (2020).
120. Z. Zong, B. He, J. Zhu, Y. Ding, W. Zhang, J. Duan, Y. Zhao, H. Chen, and Q. Tang, "Boosted hole extraction in all-inorganic $CsPbBr_3$ perovskite solar cells by interface engineering using

MoO_2/N-doped carbon nanospheres composite," Sol. Energy Mater. Sol. Cells **209**, 110460 (2020).
121. X. Li, Y. Tan, H. Lai, S. Li, Y. Chen, S. Li, P. Xu, and J. Yang, "All-inorganic $CsPbBr_3$ perovskite solar cells with 10.45% efficiency by evaporation-assisted deposition and setting intermediate energy levels," ACS Appl. Mater. Interfaces **11**, 29746–29752 (2019).
122. G. Su, B. He, Z. Gong, Y. Ding, J. Duan, Y. Zhao, H. Chen, and Q. Tang, "Enhanced charge extraction in carbon-based all-inorganic $CsPbBr_3$ perovskite solar cells by dual-function interface engineering," Electrochim. Acta **328**, 135102 (2019).
123. C. Liu, W. Li, C. Zhang, Y. Ma, J. Fan, and Y. Mai, "All-inorganic $CsPbI_2Br$ perovskite solar cells with high efficiency exceeding 13%," J. Am. Chem. Soc. **140**, 3825–3828 (2018).
124. L. Zhou, X. Guo, Z. Lin, J. Ma, J. Su, Z. Hu, C. Zhang, S. F. Liu, J. Chang, and Y. Hao, "Interface engineering of low temperature processed all-inorganic $CsPbI_2Br$ perovskite solar cells toward PCE exceeding 14%," Nano Energy **60**, 583–590 (2019).
125. L. Fu, Y. Nie, B. Li, N. Li, B. Cao, and L. Yin, "Bismuth telluride interlayer for all-inorganic perovskite solar cells with enhanced efficiency and stability," Sol. RRL **3**, 1900233 (2019).
126. X. Li, J. Yang, Q. Jiang, H. Lai, S. Li, J. Xin, W. Chu, and J. Hou, "Low-temperature solution-processed ZnSe electron transport layer for efficient planar perovskite solar cells with negligible hysteresis and improved photostability," ACS Nano **12**, 5605–5614 (2018).
127. J. Duan, Y. Zhao, B. He, and Q. Tang, "High-purity inorganic perovskite films for solar cells with 9.72% efficiency," Angew. Chem. (Int. Ed.) **130**, 3849–3853 (2018).
128. Y. Yang, T. Wang, Y. Zhang, X. Zhang, N. Li, P. Wang, Y. Qian, Q. Rong, L. Shui, and G. Zhou, "High performance all-inorganic $CsPbI_2Br$ perovskite solar cells with low energy losses," Sol. Energy **196**, 22–26 (2020).
129. L. Niu, X. Liu, C. Cong, C. Wu, D. Wu, T. R. Chang, H. Wang, Q. Zeng, J. Zhou, X. Wang, W. Fu, P. Yu, Q. Fu, S. Najmaei, Z. Zhang, B. I. Yakobson, B. K. Tay, W. Zhou, H. T. Jeng, H. Lin, T. C. Sum, C. Jin, H. He, T. Yu, and Z. Liu, "Controlled synthesis of organic/inorganic van der Waals solid for tunable light–matter interactions," Adv. Mater. **27**, 7800–7808 (2015).
130. A. Yang, J.-C. Blacton, W. Jiang, H. Zhang, J. Wong, E. Yan, Y.-R. Lin, J. Crochet, M. G. Kanatzidis, D. Jariwala, T. Low, A. D. Mohite, and H. A. Atwater, "Giant enhancement of photoluminescence emission in WS_2-two-dimensional perovskite heterostructures," Nano Lett. **19**, 4852–4860 (2019).
131. L. Zhao, Y. Gao, M. Su, Q. Shang, Z. Liu, Q. Li, Q. Wei, M. Li, L. Fu, Y. Zhong, J. Shi, J. Chen, Y. Zhao, X. Qiu, X. Liu, N. Tang, G. Xing, X. Wang, B. Shen, and Q. Zhang, "Vapor-phase incommensurate heteroepitaxy of oriented single-crystal $CsPbBr_3$ on GaN: toward integrated optoelectronic applications," ACS Nano **13**, 10085–10094 (2019).
132. S. D. Stranks, G. E. Eperon, G. Grancini, C. Menelaou, M. J. Alcocer, T. Leijtens, L. M. Herz, A. Petrozza, and H. J. Snaith, "Electron-hole diffusion lengths exceeding 1 micrometer in an organometal trihalide perovskite absorber," Science **342**, 341–344 (2013).
133. Y. Li, W. Yan, Y. Li, S. Wang, W. Wang, Z. Bian, L. Xiao, and Q. Gong, "Direct observation of long electron-hole diffusion distance in $CH_3NH_3PbI_3$ perovskite thin film," Sci. Rep. **5**, 14485 (2015).
134. J. Hu, C. Zhao, S. He, W. Tian, C. Hao, and S. Jin, "Carrier dynamics in $CsPbI_3$ perovskite microcrystals synthesized in solution phase," Chin. Chem. Lett. **29**, 699–702 (2018).
135. M. Chen, M.-G. Ju, A. D. Carl, Y. Zong, R. L. Grimm, J. Gu, X. C. Zeng, Y. Zhou, and N. P. Padture, "Cesium titanium (IV) bromide thin films based stable lead-free perovskite solar cells," Joule **2**, 558–570 (2018).
136. B. Li, H. Huang, G. Zhang, C. Yang, W. Guo, R. Chen, C. Qin, Y. Gao, V. P. Biju, A. L. Rogach, L. Xiao, and S. Jia, "Excitons and biexciton dynamics in single $CsPbBr_3$ perovskite quantum dots," J. Phys. Chem. Lett. **9**, 6934–6940 (2018).
137. R. L. Z. Hoye, L. Eyre, F. Wei, F. Brivio, A. Sadhanala, S. Sun, W. Li, K. H. L. Zhang, J. L. MacManus-Driscoll, P. D. Bristowe, R. H. Friend, A. K. Cheetham, and F. Deschler, "Fundamental carrier lifetime exceeding 1 μs in $Cs_2AgBiBr_6$ double perovskite," Adv. Mater. Interfaces **5**, 1800464 (2018).
138. F. Zhang, J. Chen, Y. Zhou, R. He, and K. Zheng, "Effect of synthesis methods on photoluminescent properties for $CsPbBr_3$ nanocrystals: hot injection method and conversion method," J. Lumin. **220**, 117023 (2020).
139. B. Yang, J. Chen, F. Hong, X. Mao, K. Zheng, S. Yang, Y. Li, T. Pullerits, W. Deng, and K. Han, "Lead-free, air-stable all-inorganic cesium bismuth halide perovskite nanocrystals," Angew. Chem. (Int. Ed.) **129**, 12645–12649 (2017).
140. K. Wu, G. Liang, Q. Shang, Y. Ren, D. Kong, and T. Lian, "Ultrafast interfacial electron and hole transfer from $CsPbBr_3$ perovskite quantum dots," J. Am. Chem. Soc. **137**, 12792–12795 (2015).
141. Q. Li and T. Lian, "Ultrafast charge separation in two-dimensional $CsPbBr_3$ perovskite nanoplatelets," J. Phys. Chem. Lett. **10**, 566–573 (2019).
142. E. M. Hutter, R. J. Sutton, S. Chandrashekar, M. Abdi-Jalebi, S. D. Stranks, H. J. Snaith, and T. J. Savenije, "Vapour-deposited cesium lead iodide perovskites: microsecond charge carrier lifetimes and enhanced photovoltaic performance," ACS Energy Lett. **2**, 1901–1908 (2017).
143. O. J. Sandberg, K. Tvingstedt, P. Meredith, and A. Armin, "Theoretical perspective on transient photovoltage and charge extraction techniques," J. Phys. Chem. C **123**, 14261–14271 (2019).
144. S. Dhariwal, L. Kothari, and S. Jain, "Theory of transient photovoltaic effects used for measurement of lifetime of carriers in solar cells," Solid-State Electron. **20**, 297–304 (1977).
145. W. M. Lin, D. Bozyigit, O. Yarema, and V. Wood, "Transient photovoltage measurements in nanocrystal-based solar cells," J. Phys. Chem. C **120**, 12900–12908 (2016).
146. S. Zhang, S. Wu, W. Chen, H. Zhu, Z. Xiong, Z. Yang, C. Chen, R. Chen, L. Han, and W. Chen, "Solvent engineering for efficient inverted perovskite solar cells based on inorganic $CsPbI_2Br$ light absorber," Mater. Today Energy **8**, 125–133 (2018).
147. D. Bai, H. Bian, Z. Jin, H. Wang, L. Meng, Q. Wang, and S. F. Liu, "Temperature-assisted crystallization for inorganic $CsPbI_2Br$ perovskite solar cells to attain high stabilized efficiency 14.81%," Nano Energy **52**, 408–415 (2018).
148. H. Guo, Y. Pei, J. Zhang, C. Cai, K. Zhou, and Y. Zhu, "Doping with $SnBr_2$ in $CsPbBr_3$ to enhance the efficiency of all-inorganic perovskite solar cells," J. Mater. Chem. C **7**, 11234–11243 (2019).
149. Y. Wang, T. Zhang, M. Kan, and Y. Zhao, "Bifunctional stabilization of all-inorganic α-$CsPbI_3$ perovskite for 17% efficiency photovoltaics," J. Am. Chem. Soc. **140**, 12345–12348 (2018).
150. C. L. Kennedy, A. H. Hill, E. S. Massaro, and E. M. Grumstrup, "Ultrafast excited-state transport and decay dynamics in cesium lead mixed halide perovskites," ACS Energy Lett. **2**, 1501–1506 (2017).
151. J. Song, Q. Cui, J. Li, J. Xu, Y. Wang, L. Xu, J. Xue, Y. Dong, T. Tian, and H. Sun, "Ultralarge all-inorganic perovskite bulk single crystal for high-performance visible–infrared dual-modal photodetectors," Adv. Opt. Mater. **5**, 1700157 (2017).